# A Stable Method for Task Priority Adaptation in Quadratic Programming via Reinforcement Learning

Andrea Testa, Marco Laghi, Edoardo del Bianco, Gennaro Raiola, Enrico Mingo Hoffman, Arash Ajoudani

# A Stable Method for Task Priority Adaptation in Quadratic Programming via Reinforcement Learning

Andrea Testa[1,2], Marco Laghi[2], Edoardo Del Bianco[1,2,3], Gennaro Raiola[1,2], Enrico Mingo Hoffman[2,4], and Arash Ajoudani[2]

***Abstract*—In emerging manufacturing facilities, robots must enhance their flexibility. They are expected to perform complex jobs, showing different behaviors on the need, all within unstructured environments, and without requiring reprogramming or setup adjustments. To address this challenge, we introduce the A3CQP, a non-strict hierarchical Quadratic Programming (QP) controller. This controller seamlessly combines both motion and interaction functionalities, with priorities dynamically and autonomously adapted through a Reinforcement Learning-based adaptation module. This module utilizes the Asynchronous Advantage Actor-Critic algorithm (A3C) to ensure rapid convergence and stable training within continuous action and observation spaces. The experimental validation, involving a collaborative peg-in-hole assembly and the polishing of a wooden plate, demonstrates the effectiveness of the proposed solution in terms of its automatic adaptability, responsiveness, and safety.**

***Index Terms*—Optimization and Optimal Control, Reinforcement Learning, Machine Learning for Robot Control.**

## I. Introduction

In recent years, the rapid advancements in robotics and automation have opened up new possibilities for enhancing industrial processes and productivity. The Industry 4.0 paradigm envisions a future where intelligent robots safely work alongside humans, seamlessly adapting to diverse tasks and dynamically adjusting their behavior to meet varying demands.

In pursuit of this vision, control architectures enabling the formulation of multiple objectives, constraints, and priorities have been developed, with Quadratic Programming (QP) as an illustrative and common example in robotics. The arrangement of the task priorities, in particular, augments robot functionality with inherent flexibility, also influencing various indirect aspects, such as human safety [1]–[3]. Nevertheless, in robotics literature, the reorganization of task importance in QP is achieved either through direct human intervention by reprogramming or through pre-established passive rules for clearly defined tasks [4], [5]. This results in limited robot autonomy, leading to poor adaptation to the multifaceted phases of intricate and unstructured jobs [6]. Furthermore, while machine learning-based strategies are well-established for controller tuning to enhance performance based on defined metrics [7]–[10], their potential for dynamically integrating diverse tasks remains largely unexplored.

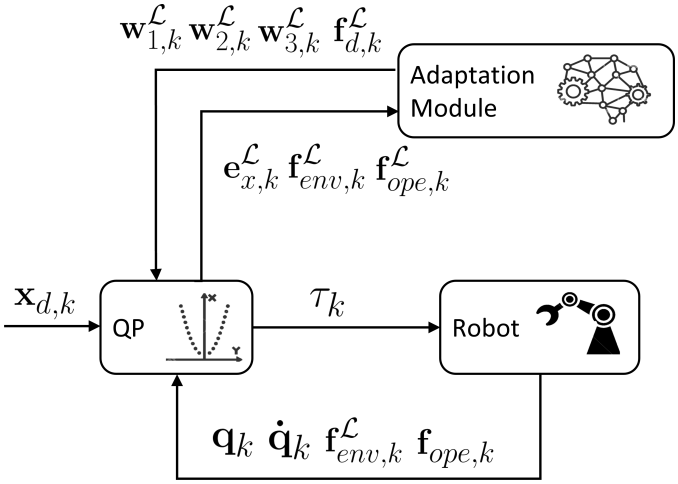


**Fig. 1:** The proposed A3CQP scheme. The QP controller at the time instant $k$ reads the joint states $\mathbf{q}_k, \dot{\mathbf{q}}_k$ and the external wrenches $\mathbf{f}_{env,k}, \mathbf{f}_{ope,k}$ from the robot interface and optimizes the joint acceleration $\ddot{\mathbf{q}}^*_k$ and wrench $\mathbf{f}^*_{d,k}$ according to the desired Cartesian pose $\mathbf{x}_{d,k}$. Using these optimal variables, the control torque $\tau_k$ is computed. The adaptation module receives the system state $\mathbf{s}_k = \{\mathbf{e}^{\mathcal{L}}_{x,k} \quad \mathbf{f}^{\mathcal{L}}_{env,k} \quad \mathbf{f}^{\mathcal{L}}_{ope,k}\}$ with respect with the frame $\mathcal{L}$ and returns the adapted weights of the QP cost function $\mathbf{w}^{\mathcal{L}}_{1,k}, \mathbf{w}^{\mathcal{L}}_{2,k}, \mathbf{w}^{\mathcal{L}}_{3,k}$, and the desired contact wrench $\mathbf{f}^{\mathcal{L}}_{d,k}$.

Based on these premises, we propose the A3CQP controller, a novel approach that harnesses the power of QP to simultaneously handle diverse tasks and constraints while dynamically modulating their weights through an adaptation module employing a Reinforcement Learning (RL) strategy, specifically the Asynchronous Advantage Actor-Critic algorithm (A3C). Our choice for A3C is due to the algorithm promising features such as fast convergence, stable training, scalability, and demonstrated robustness [11]. This seamless integration empowers the robot to stably transition between three principal tasks: Cartesian Inverse Kinematic Task, Cartesian Admittance Control Task, and Cartesian Force Control Task. These tasks can capture a broad spectrum of behaviors, ranging from precise position tracking for manipulation to exerting desired forces during physical interactions and following operator guidance for co-manipulation [12]. The automated reasoned task selection within this pool of options enables the robot to autonomously organize itself and adapt to unforeseen situations.

We summarize our contributions as follows:

[1] Leonardo S.p.A., Via Raffaele Pieragostini, 80, 16149 Genova, Italy. E-mail: {name.surname.ext}@leonardo.com
[2] Istituto Italiano di Tecnologia (IIT), Via San Quirico 19D, 16163 Genova, Italy. E-mail: {name.surname}@iit.it
[3] DISI, Università di Trento, Via Sommarive, 9, 38123 Povo, Italy. E-mail: {name.surname}@unitn.it
[4] Université de Lorraine, CNRS, Inria, LORIA, F-54000 Nancy, France. E-mail: enrico.mingo-hoffman@inria.fr

1) We introduce a *non-strict hierarchical* QP formulation where the different tasks are achieved according to the trade-off defined by their weights. This framework is crucial for generating consistent and predictable control inputs adherent to the specified constraints. Furthermore, it is decisive to ensure the demonstrated stability of the system, which plays a vital role in achieving optimal performance during operations and guaranteeing safety in interactions between the robot and the operator.
2) We present a RL-based adaptation module to dynamically adjust the weights of tasks in the QP. This module plays an essential role in imparting the robot with the capability to learn from its interactions with the environment, enabling autonomous adaptation of task priorities based on job requirements and environmental conditions.

The A3CQP controller, illustrated in Figure 1, can change the robot control mode between tasks without the need for pauses, reprogramming, or adjustments to the setup. Its versatility empowers the robot to handle multifunctional jobs, contributing to the progress of automation in industries, aligning with the vision of Industry 4.0 and 5.0 and its drive towards intelligent and adaptive manufacturing processes.

## II. Related works

After the first pioneering work on managing multiple tasks in redundant robots [13], there has been a notable surge of interest in hierarchical control. Today, in this domain, two primary approaches have been identified. The first one includes *strict hierarchies*, characterized by ordered task lists wherein the lower ones cannot interfere with the higher ones [1]. From an algorithmic point of view, this approach requires the projection of low-priority tasks in the null-space of higher-priority tasks. On the other hand, the second group examines *non-strict hierarchies*, where there is not a sharp demarcation between priority levels, and all objectives are concurrently addressed through the application of appropriate weighting [2]. This alternative approach has been suggested as more fitting and adaptable when the requirement is to dynamically adjust priorities during the transition between tasks [4], [6]. Within these frameworks, the utilization of QP optimization has become standard practice, thereby enabling the incorporation of linear constraints in both equality and inequality forms, as well as blending of strict and non-strict hierarchical techniques [14], [15].

Various strategies are employed to equip QP controllers with the capacity to adapt to dynamic environments or altered operational conditions. In [16], the authors propose a comprehensive control framework accommodating diverse parallel control modalities. Each modality addresses a different set of tasks, ordered with strict priorities. To ensure environmental compliance, the priorities remain unaltered, but a supervisor has the ability to manually switch between the control modalities. In [5], a generalized projector is presented, which can handle both strict and non-strict priorities with smooth transitions when task priorities are swapped. The evolution of task priorities over time, as well as the timing and task transitions, need to be designed manually. In [4], the weights of soft QP tasks are adjusted according to a predefined time schedule to adapt the behavior of a humanoid robot with in-contact and not-in-contact motion phases. While methodologies for automating the selection of static priorities are well-established in the literature [7], [8], [10], progress in achieving real-time updates of these priorities for unstructured tasks has been limited. In [6], time-dependent priorities are optimized offline with respect to a predetermined job. In [17], the authors propose modulating task weights online by considering the variance of demonstrated reference trajectories to mitigate incompatibilities during job execution. This method seeks to recognize instances, inferred from the variance of the demonstration, where trajectories might deviate from accurate tracking, in contrast to situations where specific critical waypoints must be traversed. However, this approach is not tailored to manage conflicts arising from inherently hierarchical task sets, and it lacks the capability to adapt to changes in the environment or job dynamics.

Broadly, the challenge of adjusting an agent's behavior in response to unfamiliar situations is often tackled using RL strategies [18]. Initially developed for discrete problems, these techniques can be extended to the continuous domain by harnessing deep learning. Within the field of RL, Actor-Critic methods stand as an amalgamation of value-based and policy-based approaches [19]. In cases where the Actor learns the action policy and the Critic estimates the value function, the resulting algorithm is known as Advantage Actor-Critic (A2C) [20]. In the context of deep learning-supported RL, it is of primary importance to decorrelate the input data [21]. To achieve such decorrelation, the most effective A2C algorithms employ multiple independent agents, each possessing their distinct weights. These agents interact in parallel with separate instances of the environment, updating the main network asynchronously. This method is known as Asynchronous Advantage Actor-Critic (A3C) [21]. However, further studies show that data decorrelation is tied more to parallel agents than asynchronous updates. Indeed, a synchronous and deterministic implementation of this algorithm, where each agent completes its segment of experience before an update is performed, achieves comparable performance to the original algorithm while providing the added benefit of improved GPU utilization efficiency [22]. In this study, we have utilized the latest implementation of the A3C algorithm as the basis for constructing the agent's decision-making policy. This implementation is employed to dynamically adjust the priorities of the QP tasks in response to evolving circumstances.

## III. QP controller architecture

This section will present a detailed description of the QP control algorithm responsible for determining the joint motor torque. Within the QP structure, we incorporate *three* distinct primary tasks that the robot controller must effectively interchange to handle multifaceted jobs like physical human-robot collaboration activities. These fundamental tasks, stacked at the same priority level of the QP, are listed below.

1) The Cartesian Inverse Kinematic Task (IK) is responsible for driving the manipulator toward the desired targets during unrestricted motion while ensuring safe compliance with the environment.
2) The Cartesian Admittance Control Task (AC) is essential for physical human-robot collaboration, allowing the robot to follow the guidance provided by the operator.
3) The Cartesian Force Control Task (FC) allows the application of precise desired forces when the robot enters in contact with the target workpieces or work surfaces.

During various phases of the job, such as operator guidance, workpiece interaction, or free motion, these tasks must be seamlessly activated to adjust the behavior of the robot accordingly. Throughout the IK task, it is desirable to prevent the robot from encountering singularities and to maintain a high degree of manipulability as it follows the Cartesian reference trajectory. To achieve this, we introduce an additional task called the Joint-level Control Task (JC) at the same priority level in the QP. The JC task is activated alongside the IK task and is designed to optimize the robot joint configuration within its nullspace. The variables to be optimized at each control step $k$ include the joint accelerations $\ddot{\mathbf{q}}_k \in \mathbb{R}^n$, and the Cartesian wrench exerted by the end effector $\mathbf{f}_k \in \mathbb{R}^6$. In the event of contact, this wrench acts in opposition to the external one. The control problem is formulated as the following QP:

$$\begin{aligned}\min_{\ddot{\mathbf{q}}_k,\mathbf{f}_k} \; & \| \overbrace{\mathbf{J}_k\ddot{\mathbf{q}}_k + \dot{\mathbf{J}}_k\dot{\mathbf{q}}_k - \ddot{\mathbf{x}}_{d,k}}^{\text{IK task}} \|_{\mathbf{w}_1} + \| \overbrace{\mathbf{f}_k - \mathbf{f}_{adm,k}}^{\text{AC task}} \|_{\mathbf{w}_2} + \\ & \| \underbrace{\mathbf{f}_k - \mathbf{f}_{ctc,k}}_{\text{FC task}} \|_{\mathbf{w}_3} + \| \underbrace{\ddot{\mathbf{q}}_k - \ddot{\mathbf{q}}_{d,k}}_{\text{JC task}} \|_{\epsilon\mathbf{J}_k^T\mathbf{w}_1\mathbf{J}_k}; \\ \text{s.t.} \quad & \underline{\ddot{\mathbf{q}}} \le \ddot{\mathbf{q}}_k \le \bar{\ddot{\mathbf{q}}}; \\ & \underline{\mathbf{f}} \le \mathbf{f}_k \le \bar{\mathbf{f}},\end{aligned} \tag{1}$$

with $\mathbf{J}_k, \dot{\mathbf{J}}_k \in \mathbb{R}^{6\times n}$ the end effector Jacobian and its time derivative, $\dot{\mathbf{q}}_k \in \mathbb{R}^n$ the joint velocities. $\underline{\ddot{\mathbf{q}}}, \bar{\ddot{\mathbf{q}}} \in \mathbb{R}^n$ and $\underline{\mathbf{f}}, \bar{\mathbf{f}} \in \mathbb{R}^6$ represent the lower and upper bounds, respectively, for the optimization variables. Regarding the target vectors, $\ddot{\mathbf{q}}_{d,k} \in \mathbb{R}^n$ denotes the reference joint accelerations, $\ddot{\mathbf{x}}_{d,k} \in \mathbb{R}^6$ represents the desired Cartesian end effector acceleration, while $\mathbf{f}_{adm,k}, \mathbf{f}_{ctc,k} \in \mathbb{R}^6$ are the desired admittance and contact wrenches, respectively. $\mathbf{w}_1, \mathbf{w}_2, \mathbf{w}_3 \in \mathbb{R}^{6\times 6}$ are weight matrices used to indicate the relative importance of the first three tasks. On the other hand, the scalar $\epsilon$ determines the relationship between the IK and the JC tasks. By choosing $\epsilon \ll 1$, the IK task is prioritized while the JC task serves as a regularization mechanism. Section 3.5 of the book [23] demonstrates that minimizing the quadratic norm of the vector $\ddot{\mathbf{q}}_k - \ddot{\mathbf{q}}_{d,k}$, subject to a Cartesian constraint in the form $\mathbf{J}_k\ddot{\mathbf{q}}_k + \dot{\mathbf{J}}_k\dot{\mathbf{q}}_k = \ddot{\mathbf{x}}_{d,k}$, achieves norm minimization in the nullspace as a secondary task. Including both terms in the optimization process and scaling them by $\epsilon$ yields a similar effect. The solutions sought primarily aim to reach the desired Cartesian target, with a secondary objective to follow the reference acceleration $\ddot{\mathbf{q}}_{d,k}$, computed to prevent the robot from adopting unfavorable joint configurations near singularities.

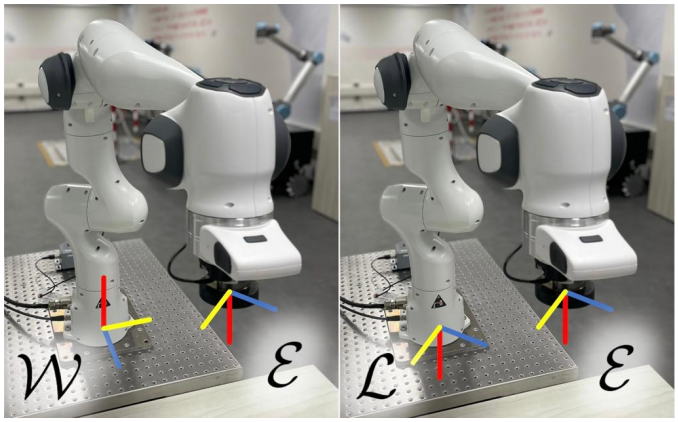


**Fig. 2:** Representation of the Cartesian reference frames $\mathcal{W}$, $\mathcal{L}$, and $\mathcal{E}$.

The Cartesian variables in (1) are expressed with respect to the world reference frame $\mathcal{W}$. However, in this study, we will consistently define the desired wrenches based on a local reference frame $\mathcal{L}$ centered in $\mathcal{W}$ but aligned with the end effector $\mathcal{E}$ of the robot. This is convenient because the adaptation module, responsible for changing task priorities, adopts the perspective of the end effector. The reference frames introduced are shown in Figure 2. The transformation of wrenches from $\mathcal{W}$ to $\mathcal{L}$ is

$$\mathbf{f}^{\mathcal{L}}_{adm,k} = {}^{\mathcal{W}}D^T_{\mathcal{L},k}\ \mathbf{f}_{adm,k}; \quad \mathbf{f}^{\mathcal{L}}_{ctc,k} = {}^{\mathcal{W}}D^T_{\mathcal{L},k}\ \mathbf{f}_{ctc,k}, \tag{2}$$

with ${}^{\mathcal{W}}D_{\mathcal{L},k} \in \mathbb{R}^{6\times 6}$ being the Adjoint matrix associated to the homogeneous transformation matrix of $\mathcal{L}$ with respect to $\mathcal{W}$ at control step $k$. Since $\mathcal{L}$ and $\mathcal{W}$ share the same origin, ${}^{\mathcal{W}}D_{\mathcal{L},k}$ always results in a block-diagonal matrix constructed based on the rotation matrix ${}^{\mathcal{W}}R_{\mathcal{L},k} \in \mathbb{R}^{3\times 3}$:

$${}^{\mathcal{W}}D_{\mathcal{L},k} = \begin{bmatrix} {}^{\mathcal{W}}R_{\mathcal{L},k} & 0 \\ 0 & {}^{\mathcal{W}}R_{\mathcal{L},k} \end{bmatrix}. \tag{3}$$

In the optimal control problem (1), the IK and JC tasks are responsible for computing the optimal acceleration $\ddot{\mathbf{q}}^*_k$, while the optimal wrench $\mathbf{f}^*_k$ is obtained from the AC and FC tasks. These computed values determine the desired joint motor torque at time instant $k$, as determined by the equation derived from the computed-torque control paradigm, described in Section 8.6 of the book [24]:

$$\boldsymbol{\tau}_k = \mathbf{B}_k(\ddot{\mathbf{q}}^*_k + \ddot{\mathbf{q}}_{pd,k}) + \mathbf{J}^T_k\mathbf{f}^*_k + \mathbf{h}_k + \mathbf{g}_k; \tag{4}$$

$$\ddot{\mathbf{q}}_{pd,k} = \mathbf{J}^T_k\mathbf{w}_1\mathbf{J}_k\left(c_v(\dot{\mathbf{q}}^*_k - \dot{\mathbf{q}}_k) + c_p(\mathbf{q}^*_k - \mathbf{q}_k)\right). \tag{5}$$

Here, $\mathbf{B}_k \in \mathbb{R}^{n\times n}$ represents the joint inertia matrix, $\mathbf{h}_k \in \mathbb{R}^n$ corresponds to the Coriolis and centrifugal term, and $\mathbf{g}_k \in \mathbb{R}^n$ is the gravitational term. The feedback joint acceleration, denoted as $\ddot{\mathbf{q}}_{pd,k}$, is calculated by summing the derivative and proportional feedback terms, which are scaled by the scalar gains $c_v$ and $c_p$, respectively. $\dot{\mathbf{q}}_k, \mathbf{q}_k \in \mathbb{R}^n$ represent the measured joint velocity and position, while the desired variables $\dot{\mathbf{q}}^*_k, \mathbf{q}^*_k \in \mathbb{R}^n$ are obtained by integrating $\ddot{\mathbf{q}}^*_k$ as follows:

$$\dot{\mathbf{q}}^*_k = \dot{\mathbf{q}}^*_{k-1} + \Delta t\ddot{\mathbf{q}}^*_k; \tag{6}$$

$$\mathbf{q}^*_k = \mathbf{q}^*_{k-1} + \Delta t\dot{\mathbf{q}}^*_{k-1} + \tfrac{\Delta t^2}{2}\ddot{\mathbf{q}}^*_k. \tag{7}$$

Since the feedback acceleration plays a role in ensuring the tracking of desired joint positions and velocities, which are computed based on IK and JC tasks, this term should only be active when these tasks are in operation. Therefore, it is scaled using the same weight matrix $\mathbf{w}_1$. Furthermore, as detailed in Subsection III-B, the joint acceleration limits $\underline{\ddot{\mathbf{q}}}, \bar{\ddot{\mathbf{q}}}$, which also consider velocity and position constraints, ensure that the desired variables $\dot{\mathbf{q}}_k^*, \mathbf{q}_k^*$ adhere to these limits. Consequently, the resulting acceleration $\ddot{\mathbf{q}}_k^* + \ddot{\mathbf{q}}_{pd,k}$ remains feasible.

In the following paragraphs, we will delve into the definition of problem (1), specifically focusing on the management of task weights, the constraints, and the generation of references. Once the details have been defined, we will proceed to discuss the stability of the control framework.

### A. Task weights

To effectively handle the four concurrent tasks and determine their trade-off for each degree of freedom, we need to assign weights that reflect their relevance. For this purpose, we begin by using three weight diagonal matrices $\mathbf{w}_1^{\mathcal{L}}, \mathbf{w}_2^{\mathcal{L}}, \mathbf{w}_3^{\mathcal{L}}$. These matrices represent the relative importance of the IK, AC, and FC tasks, respectively, for each Cartesian degree of freedom in the local reference frame $\mathcal{L}$. The diagonal elements of these matrices are determined and updated online using the intelligent adaptation algorithm described in Section IV. These terms are adjusted as $\mathcal{C}^0$ functions to ensure a continuous transition in the optimal control problem (1). It is important to note that the sum of the diagonal elements pertaining to the same degree of freedom always equals 1 (e.g., for the local z-axis, $w_1^{\mathcal{L},z} + w_2^{\mathcal{L},z} + w_3^{\mathcal{L},z} = 1$). This implies that certain elements in this sum may be zero, indicating that the adaptation module deems these tasks as insignificant. For instance, when $w_3^{\mathcal{L},z} = 0$, the FC task along the local z-axis is considered irrelevant. However, the simultaneous deactivation of all the tasks associated with a particular degree of freedom (e.g., the AC and FC tasks for $\mathbf{f}_z^{\mathcal{L}}$, or the IK and JC tasks for $\ddot{\mathbf{x}}_y^{\mathcal{L}}$) does not make the associated optimal control problem indeterminate, as the resulting QP Hessians are regularized. Therefore, the optimization variable not associated with any active task is set to null as a result of problem resolution. Since the Cartesian variables in the tasks are expressed in the world frame $\mathcal{W}$, it is necessary to rotate the local diagonal matrices as follows:

$$\begin{aligned} \mathbf{w}_1 = {}^{\mathcal{W}}D_{\mathcal{L}}\ \mathbf{w}_1^{\mathcal{L}}\ {}^{\mathcal{W}}D_{\mathcal{L}}^T; \quad \mathbf{w}_2 = {}^{\mathcal{W}}D_{\mathcal{L}}\ \mathbf{w}_2^{\mathcal{L}}\ {}^{\mathcal{W}}D_{\mathcal{L}}^T; \\ \mathbf{w}_3 = {}^{\mathcal{W}}D_{\mathcal{L}}\ \mathbf{w}_3^{\mathcal{L}}\ {}^{\mathcal{W}}D_{\mathcal{L}}^T. \end{aligned} \tag{8}$$

The resulting matrices $\mathbf{w}_1, \mathbf{w}_2, \mathbf{w}_3$ are non-diagonal, symmetric and positive-definite.

### B. Constraints

To ensure that the robot does not exert excessive force, we constrain the wrench to respect the limits $\mathbf{f}_{max}, \mathbf{f}_{min}$. Additionally, during contact phases, we aim to optimize a feasible wrench that observes the friction cone. We implement this constraint as

$$\mathbf{U}(\mu)\mathbf{f}_k^* \leq 0, \tag{9}$$

where the matrix $\mathbf{U} \in \mathbb{R}^{4\times 6}$, which depends on the friction coefficient $\mu$, represents the linearized friction cone in the case of single contact point [25]. The final boundaries, $\underline{\mathbf{f}}$ and $\bar{\mathbf{f}}$, are determined by selecting the most limiting conditions.

When considering the joint acceleration limits $\underline{\ddot{\mathbf{q}}}, \bar{\ddot{\mathbf{q}}}$, it is necessary to account for velocity and position constraints. Merely constraining the integrals of the controlled variables is inadequate to ensure that the resulting integral values remain within acceptable boundaries. This traditional approach can ensure feasibility between control bounds and imposed integral constraints only when they have a relative degree of 1. So, in our scenario, the position limits would not be respected. To fulfill all constraints within an instantaneous controller, we adopt a methodology rooted in the invariance control approach [26], which has demonstrated superior performance when compared to other state-of-the-art methods in this field [27].

### C. References

In total, four references need to be generated, one for each cost term that makes up the cost function of the QP controller (1). In the following, we explain the definition of each of them.

*1) IK task reference:* The desired Cartesian acceleration $\ddot{\mathbf{x}}_{d,k}$ is computed as

$$\ddot{\mathbf{x}}_{d,k} = \mathbf{K}_p \mathbf{e}_{x,k} - \mathbf{K}_v \dot{\mathbf{x}}. \tag{10}$$

In this equation, $\mathbf{e}_{x,k} = \mathbf{x}_{d,k} \ominus \mathbf{x}_k$ represents the Cartesian pose error, where $\mathbf{x}_{d,k}, \mathbf{x}_k \in \mathbb{R}^3 \times \mathcal{S}^3$ are the desired and measured end effector Cartesian poses, respectively. These poses belong to the Lie group $\mathbb{R}^3 \times \mathcal{S}^3$, as we represent their translation part as vectors in $\mathbb{R}^3$ and their rotation part as quaternions in $\mathcal{S}^3$. Their difference $\mathbf{e}_{x,k} \in \mathbb{R}^6$ is a 6-dimensional vector since the rotation part is converted to the axis-angle representation. Furthermore, the Cartesian velocity, with respect to the frame $\mathcal{W}$, can be expressed as a vector in the Euclidean space $\mathbb{R}^6$, which is isomorphic to the Lie Algebra of the group [28]. The gains $\mathbf{K}_p, \mathbf{K}_v \in \mathbb{R}^{6\times 6}$ are defined as

$$\begin{aligned} \mathbf{K}_p &= \begin{bmatrix} k_p \mathbf{I}_{3\times 3} & 0 \\ 0 & k_\theta \mathbf{I}_{3\times 3} \end{bmatrix}; \\ \mathbf{K}_v &= \begin{bmatrix} 2\sqrt{k_p}\mathbf{I}_{3\times 3} & 0 \\ 0 & 2\sqrt{k_\theta}\mathbf{I}_{3\times 3} \end{bmatrix}, \end{aligned} \tag{11}$$

and determine the acceleration according to the position and the velocity error. Using these matrices, we establish the reference acceleration to match that of a desired second-order dynamic system critically damped. Consequently, we can interpret the IK task as a Cartesian Impedance control task.

Therefore, the dynamics of the closed-loop system when the IK task is active can be described by considering the control torque expression (4) and the original dynamics of the manipulator in Cartesian space, represented by the equation

$$\mathbf{\Lambda}_k(\ddot{\mathbf{x}}_k - \dot{\mathbf{J}}_k \dot{\mathbf{q}}_k) + \mathbf{C}_k \dot{\mathbf{x}}_k + \hat{\mathbf{g}}_k = \mathbf{J}_k^{T^\dagger} \boldsymbol{\tau}_k + \mathbf{f}_{ext,k}. \tag{12}$$

Here, $\mathbf{\Lambda}_k, \mathbf{C}_k \in \mathbb{R}^{6\times 6}$ are respectively the Cartesian inertia and Coriolis matrices, $\hat{\mathbf{g}}_k \in \mathbb{R}^6$ denotes the Cartesian gravitational force, $\mathbf{J}_k^{T^\dagger} = \mathbf{\Lambda}^T \mathbf{J} \mathbf{B}^{-1^T} \in \mathbb{R}^{6\times n}$ indicates the dynamic consistent pseudo-inverse of the transposed Jacobian [29], and

$\mathbf{f}_{ext,k}$ indicates the external wrench. By substituting $\boldsymbol{\tau}_k$ with (4) and noting that $\mathbf{f}_k^* = 0$ because we are optimizing only the desired joint acceleration $\ddot{\mathbf{q}}_k^*$, the Cartesian dynamics (12) simplifies to

$$\boldsymbol{\Lambda}_k \ddot{\mathbf{x}}_k = \boldsymbol{\Lambda}_k(\ddot{\mathbf{x}}_{d,k} + \ddot{\mathbf{x}}_{pd,k}) + \mathbf{f}_{ext,k}, \tag{13}$$

where the feedback acceleration $\ddot{\mathbf{x}}_{pd,k} \in \mathbb{R}^6$ is defined as

$$\ddot{\mathbf{x}}_{pd,k} = \mathbf{J}_k \left( c_v(\dot{\mathbf{q}}_k^* - \dot{\mathbf{q}}_k) + c_p(\mathbf{q}_k^* - \mathbf{q}_k) \right). \tag{14}$$

Finally, by formulating the reference acceleration as in (10), we arrive at the dynamics of the closed-loop system:

$$\boldsymbol{\Lambda}_k \left( \ddot{\mathbf{x}}_k + \mathbf{K}_v \dot{\mathbf{x}}_k + \mathbf{K}_p(-\mathbf{e}_{x,k}) + \ddot{\mathbf{x}}_{pd,k} \right) = \mathbf{f}_{ext,k}; \tag{15}$$

This description captures the system behavior when only the IK task is active.

*2) AC task reference:* The desired admittance force $\mathbf{f}_{adm,k}$ combines with the operator's force to guide the manipulator towards the desired posture. This active contribution ensures compliance with the operator's intentions and reduces the effort required for interaction. To determine the desired reference for the admittance force, we need to compare the desired dynamics with the closed-loop system dynamics when the AC task is active. Therefore, we examine the baseline equation for Cartesian dynamics (12) and the control torque (4). In this context, we set $\ddot{\mathbf{q}}_k^* = \ddot{\mathbf{q}}_{pd,k} = 0$ as our focus is currently on optimizing only the desired wrench $\mathbf{f}_k^*$. By combining these two equations, we arrive at the following expression:

$$\boldsymbol{\Lambda}_k(\ddot{\mathbf{x}}_k - \dot{\mathbf{J}}_k \dot{\mathbf{q}}_k) = \mathbf{f}_k^* + \mathbf{f}_{ext,k}. \tag{16}$$

In order to obtain the desired response closed-loop dynamics

$$\boldsymbol{\Lambda}_d \ddot{\mathbf{x}}_k + \mathbf{C}_d \dot{\mathbf{x}}_k = \mathbf{f}_{ext,k}, \tag{17}$$

where $\boldsymbol{\Lambda}_d = \Lambda_d \mathbf{I}_{6\times6}$, $\mathbf{C}_d = C_d \mathbf{I}_{6\times6}$ are the desired Cartesian inertia and damping matrices, respectively, the admittance force must be

$$\mathbf{f}_{adm,k} = \mathbf{f}_k^* = \left( [\boldsymbol{\Lambda}_k \boldsymbol{\Lambda}_d^{-1}] - \mathbf{I}_{6\times6} \right) \mathbf{f}_{ext,k} - (\mathbf{C}_d \mathbf{J}_k + \boldsymbol{\Lambda}_k \dot{\mathbf{J}}_k)\dot{\mathbf{q}}_k, \tag{18}$$

or, alternatively,

$$\mathbf{f}_{adm,k} = \mathbf{f}_k^* = \boldsymbol{\Lambda}_k(\ddot{\mathbf{x}}_k - \dot{\mathbf{J}}_k \dot{\mathbf{q}}_k) - \boldsymbol{\Lambda}_d \ddot{\mathbf{x}}_k - (\mathbf{C}_d \mathbf{J}_k + \boldsymbol{\Lambda}_k \dot{\mathbf{J}}_k)\dot{\mathbf{q}}_k. \tag{19}$$

We have opted to use the formulation (18) in order to avoid the need to calculate the Cartesian acceleration $\ddot{\mathbf{x}}_k$. Additionally, the diagonal structure of the desired inertia matrix $\boldsymbol{\Lambda}_d$ simplifies the matrix inversion process.

*3) FC task reference:* The desired contact force $\mathbf{f}_{ctc,k}$ is obtained by applying the required local contact force, $\mathbf{f}_{d,k}^{\mathcal{L}}$, chosen by the autonomous environment adaptation policy, to the transformation (3):

$$\mathbf{f}_{ctc,k} = {}^{\mathcal{W}}D_{\mathcal{L}} \ \mathbf{f}_{d,k}^{\mathcal{L}} \in \mathbb{R}^6. \tag{20}$$

The local contact force $\mathbf{f}_{d,k}^{\mathcal{L}}$ is updated online according to $\mathcal{C}^0$ continuity constraints and is limited to the maximum value

$$\mathbf{f}_{d,k}^{\mathcal{L}} \leq \bar{\mathbf{f}}_d^{\mathcal{L}}. \tag{21}$$

By incorporating (20) into (16), we obtain the closed-loop system dynamics when the FC task is active:

$$\boldsymbol{\Lambda}_k(\ddot{\mathbf{x}}_k - \dot{\mathbf{J}}_k \dot{\mathbf{q}}_k) = {}^{\mathcal{W}}D_{\mathcal{L}} \ \mathbf{f}_{d,k}^{\mathcal{L}} + \mathbf{f}_{ext,k}. \tag{22}$$

*4) JC task reference:* Finally, we compute the desired joint acceleration $\ddot{\mathbf{q}}_d$ as

$$\ddot{\mathbf{q}}_d = k_q \mathbf{e}_{q,k} - 2\sqrt{k_q}\dot{\mathbf{q}}_k, \tag{23}$$

where $\mathbf{e}_{q,k} = \mathbf{q}_d - \mathbf{q}_k$ represents the joint position error, with $\mathbf{q}_d$ a convenient joint configuration chosen to be far from the joint limits and singularities. $k_q$ is a scalar gain.

After establishing the four control references as explained earlier, we can substitute them into (1), leading to the final formulation of the control problem, represented by (24). This problem can be separated into two distinct single-variable sub-problems. The first sub-problem (24a) is responsible for determining the optimal joint acceleration $\ddot{\mathbf{q}}_k^*$, while the second sub-problem (24b) focuses on finding the optimal wrench $\mathbf{f}_k^*$.

$$\begin{aligned}
\min_{\ddot{\mathbf{q}}_k} \ & \overbrace{\frac{1}{2}\ddot{\mathbf{q}}_k^T \mathbf{J}_k^T \mathbf{w}_1 \mathbf{J}_k \ddot{\mathbf{q}}_k + \ddot{\mathbf{q}}_k^T \mathbf{J}_k^T \mathbf{w}_1 \dot{\mathbf{J}}_k \dot{\mathbf{q}}_k}^{\text{IK task}} - \\
& \ddot{\mathbf{q}}_k^T \mathbf{J}_k^T \mathbf{w}_1 \left( \mathbf{K}_p \mathbf{e}_{x,k} - \mathbf{K}_v \dot{\mathbf{x}}_k \right) + \\
& \overbrace{\frac{1}{2}\ddot{\mathbf{q}}_k^T \mathbf{J}_k^T \epsilon \mathbf{w}_1 \mathbf{J}_k \ddot{\mathbf{q}}_k - \ddot{\mathbf{q}}_k^T \mathbf{J}_k^T \epsilon \mathbf{w}_1 \mathbf{J}_k \left( k_q \mathbf{e}_{q,k} - 2\sqrt{k_q}\dot{\mathbf{q}}_k \right)}^{\text{JC task}}; \\
\text{s.t.} \ & \\
& \underline{\ddot{\mathbf{q}}} \leq \ddot{\mathbf{q}}_k \leq \bar{\ddot{\mathbf{q}}}.
\end{aligned} \tag{24a}$$

$$\begin{aligned}
\min_{\mathbf{f}_k} \ & \overbrace{\frac{1}{2}\mathbf{f}_k^T \mathbf{w}_2 \mathbf{f}_k - \mathbf{f}_k^T \mathbf{w}_2 \left( [\boldsymbol{\Lambda}_k \boldsymbol{\Lambda}_d^{-1}] - \mathbf{I}_{6\times6} \right) \mathbf{f}_{ext,k}}^{\text{AC task}} + \\
& \mathbf{f}_k^T \mathbf{w}_2 (\mathbf{C}_d \mathbf{J}_k + \boldsymbol{\Lambda}_k \dot{\mathbf{J}}_k)\dot{\mathbf{q}}_k + \\
& \underbrace{\frac{1}{2}\mathbf{f}_k^T \mathbf{w}_3 \mathbf{f}_k - \mathbf{f}_k^T \mathbf{w}_3 \mathbf{f}_{ctc,k}}_{\text{FC task}}; \\
\text{s.t.} \ & \\
& \underline{\mathbf{f}} \leq \mathbf{f}_k \leq \bar{\mathbf{f}}.
\end{aligned} \tag{24b}$$

Examining the stability of the solution to this optimal control problem is a crucial aspect of its performance evaluation. This systematic analysis ensures robustness against unforeseen external disturbances, guaranteeing a consistent level of performance. The evaluation has been conducted in Appendix A. Stability has been demonstrated without imposing specific conditions on the task weights. However, it is crucial to restrict the desired contact force $\mathbf{f}_{d,k}^{\mathcal{L}}$ from aligning with the end effector Cartesian velocity $\dot{\mathbf{x}}_k$, preventing the system from generating power. This requirement must be addressed by the adaptation module.

## IV. Adaptation Module

This section presents a comprehensive description of the adaptation module implemented to dynamically adjust the behaviour of the robot. As mentioned earlier, this automatic policy directly works on the QP parameters, enabling the robot to adapt to the job requirements by updating the task priorities.

It employs a RL strategy to dynamically select the local weight matrices $\mathbf{w}_{1,k}^{\mathcal{L}}, \mathbf{w}_{2,k}^{\mathcal{L}}, \mathbf{w}_{3,k}^{\mathcal{L}}$ and the most appropriate local contact force $\mathbf{f}_{d,k}^{\mathcal{L}}$, based on the continuous observed state $\mathbf{s}_k \in \mathbb{R}^{18}$. The latter is defined as

$$\mathbf{s}_k = \begin{pmatrix} \mathbf{e}_{x,k}^{\mathcal{L}} & \mathbf{f}_{env,k}^{\mathcal{L}} & \mathbf{f}_{ope,k}^{\mathcal{L}} \end{pmatrix}, \tag{25}$$

where, in addition to the previously defined error pose $\mathbf{e}_{x,k}$, we have the external forces originating from contact with the environment, denoted as $\mathbf{f}_{env,k}^{\mathcal{L}} \in \mathbb{R}^6$, and the external forces exerted by the operator, represented as $\mathbf{f}_{ope,k}^{\mathcal{L}} \in \mathbb{R}^6$. The RL algorithm is specialized for a particular axis of the local frame $\mathcal{L}$. Therefore, the observed state, represented by three 6-dimensional vectors, is processed by six distinct agents, each responsible for handling one direction, corresponding to a set of three scalars. Hence, at each time step $k$, an agent receives the normalized state

$$\tilde{s}_k = \begin{Bmatrix} \frac{|e_{x,k}^{\mathcal{L}}|}{\bar{e}_x^{\mathcal{L}}} & \frac{|f_{env,k}^{\mathcal{L}}|}{\bar{f}_{env}^{\mathcal{L}}} & \frac{|f_{ope,k}^{\mathcal{L}}|}{\bar{f}_{ope}^{\mathcal{L}}} \end{Bmatrix} \in \mathbb{R}^3, \tag{26}$$

with the elements being normalized to enhance learning stability. On the basis of $\tilde{s}_k$, the agent determines an action denoted as:

$$a_k = \begin{Bmatrix} \dot{w}_{1,k}^{\mathcal{L}} & \dot{w}_{2,k}^{\mathcal{L}} & \dot{w}_{3,k}^{\mathcal{L}} & \dot{f}_{d,k}^{\mathcal{L}} \end{Bmatrix} \in \mathbb{R}^4; \tag{27a}$$

$$\dot{w}_{1,k}^{\mathcal{L}}, \dot{w}_{2,k}^{\mathcal{L}}, \dot{w}_{3,k}^{\mathcal{L}}, \dot{f}_{d,k}^{\mathcal{L}} \in [-1, 1], \tag{27b}$$

representing the selected rate of change for task priorities and the desired contact force. This action (27a) is selected according to the agent's policy $\pi$, which maps states $\tilde{s}_k$ to actions $a_k$. In response to the action, the agent receives the subsequent state $\tilde{s}_{k+1}$ and a scalar reward $r_k$. While the rate of change can be discontinuous, as there are no constraints on the difference between two consecutive actions (e.g., $a_k - a_{k-1}$), the resulting module output, defined as

$$o_k = \begin{Bmatrix} w_{1,k}^{\mathcal{L}} & w_{2,k}^{\mathcal{L}} & w_{3,k}^{\mathcal{L}} & f_{d,k}^{\mathcal{L}} \end{Bmatrix} \in \mathbb{R}^4; \tag{28a}$$

$$w_{1,k}^{\mathcal{L}}, w_{2,k}^{\mathcal{L}}, w_{3,k}^{\mathcal{L}} \in [0, 1]; \tag{28b}$$

$$w_{1,k}^{\mathcal{L}} + w_{2,k}^{\mathcal{L}} + w_{3,k}^{\mathcal{L}} = 1, \tag{28c}$$

is $\mathcal{C}^0$, and is calculated using the following equations:

$$\breve{w}_{1,k}^{\mathcal{L}} = \breve{w}_{1,k-1}^{\mathcal{L}} + \sigma_w \Delta t \dot{w}_{1,k}^{\mathcal{L}} \text{ if } -\tfrac{\sigma_w}{2} \leq \breve{w}_{1,k}^{\mathcal{L}} \leq \tfrac{\sigma_w}{2}; \tag{29a}$$

$$\breve{w}_{2,k}^{\mathcal{L}} = \breve{w}_{2,k-1}^{\mathcal{L}} + \sigma_w \Delta t \dot{w}_{2,k}^{\mathcal{L}} \text{ if } -\tfrac{\sigma_w}{2} \leq \breve{w}_{2,k}^{\mathcal{L}} \leq \tfrac{\sigma_w}{2}; \tag{29b}$$

$$\breve{w}_{3,k}^{\mathcal{L}} = \breve{w}_{3,k-1}^{\mathcal{L}} + \sigma_w \Delta t \dot{w}_{3,k}^{\mathcal{L}} \text{ if } -\tfrac{\sigma_w}{2} \leq \breve{w}_{3,k}^{\mathcal{L}} \leq \tfrac{\sigma_w}{2}; \tag{29c}$$

$$f_{d,k}^{\mathcal{L}} = f_{d,k-1}^{\mathcal{L}} + \sigma_f \Delta t \dot{f}_{d,k}^{\mathcal{L}} \quad \text{if } 0 \leq f_{d,k}^{\mathcal{L}} \leq \bar{f}_d^{\mathcal{L}}; \tag{29d}$$

$$w_{1,k}^{\mathcal{L}} = \frac{\exp \breve{w}_{1,k}^{\mathcal{L}}}{\sum_{i=1}^{3} \exp \breve{w}_{i,k}^{\mathcal{L}}}; \quad w_{2,k}^{\mathcal{L}} = \frac{\exp \breve{w}_{2,k}^{\mathcal{L}}}{\sum_{i=1}^{3} \exp \breve{w}_{i,k}^{\mathcal{L}}};$$

$$w_{3,k}^{\mathcal{L}} = \frac{\exp \breve{w}_{3,k}^{\mathcal{L}}}{\sum_{i=1}^{3} \exp \breve{w}_{i,k}^{\mathcal{L}}}. \tag{29e}$$

In this context, scalar parameters $\sigma_w$ and $\sigma_f$ are employed to adjust the rate of change of the variables in $o_k$ according to the desired system responsiveness. They also define upper and lower limits to bound $\breve{w}_{i,k}^{\mathcal{L}}$, which represents the weights before the normalization process executed by the softmax function (29e). This ensures compliance with the constraints (28b) and (28c).

In the following paragraphs, we will provide a detailed explanation of the RL algorithm used in this study. We will specify the reward function chosen, explain the RL methods employed, and describe the approach used to tune the various hyperparameters of the algorithm.

### *A. Reward function*

The reward received at each learning step plays a crucial role in assessing the current behavior of the robot and guiding it towards appropriate actions. In our scenario, this function involves the three terms of the normalized state variables defined in (26), providing a metric for the desirability of each region in the state-space. In many applications where collaborative robots are employed today, three key and general objectives can be identified.

- The first objective is to reach the target position by minimizing the positional error $e_{x,k}$ relative to the target location for picking or working.
- The second objective arises when an operator physically interacts with the robot. Here, the robot must minimize the external force exerted by the operator $f_{ope,k}$ to align with the operator's intentions while minimizing resistance and maximizing compliance.
- The third objective comes into play when the robot has to interact with the workspace, sensing an environmental contact force $f_{env,k}$. The control of the force exerted in this contact is crucial for the successful execution of various practical tasks where the end-effector needs to manipulate an object or perform operations on a surface. Typical examples in industrial settings encompass activities such as polishing, deburring, machining, or assembly. The execution of these tasks with only motion control would be feasible only if an accurate geometric model is available.

The agent needs to shape its policy by balancing these three general requirements. To effectively achieve this, we define the reward function as a sum of four terms:

$$r_k = \sum_{i=1}^{4} \hat{r}_{i,k}; \tag{30a}$$

$$\hat{r}_{1,k} = -\alpha_1 \frac{|e_{x,k}^{\mathcal{L}}|}{\bar{e}_x^{\mathcal{L}}}; \tag{30b}$$

$$\hat{r}_{2,k} = -\alpha_2 \frac{|f_{ope,k}^{\mathcal{L}}|}{\bar{f}_{ope}^{\mathcal{L}}}; \tag{30c}$$

$$\hat{r}_{3,k} = \alpha_3 \frac{|f_{env,k}^{\mathcal{L}}|}{\bar{f}_{env}^{\mathcal{L}}}; \tag{30d}$$

$$\hat{r}_{4,k} = -\alpha_4 \frac{f_{d,k}^{\mathcal{L}}}{\bar{f}_{d,k}^{\mathcal{L}}}. \tag{30e}$$

Here, $\alpha_1, \alpha_2, \alpha_3$, and $\alpha_4$ represent the positive weights assigned to each term. All the variables have been normalized within the range of $[0, 1]$. In the following list, the purpose of each reward term is described.

- The first term (30b) discourages significant positional errors between the present manipulator coordinate and the target, encouraging the robot to address the primary objective. It assigns a negative value to states farther from the target, prompting an increase in $w_{1,k}^{\mathcal{L}}$ accordingly.
- The second term (30c) penalizes large forces applied by the operator, caused by intense collaboration effort resulting from the reactive response of the robot. This term

is crucial for achieving the second objective, promoting the activation of the AC task by increasing $w^{\mathcal{L}}_{2,k}$ when needed.
- The third term (30d) incentivizes the robot to enhance its interaction force with the environment by increasing $w^{\mathcal{L}}_{3,k}$. This helps the robot to establish contact with the target workpiece or worksurface when required.
- The fourth term (30e) penalizes a nonzero desired contact force. This prompts the robot to increase $f^{\mathcal{L}}_{d,k}$ only when in contact, i.e., when the penalty is outweighed by the beneficial effect resulting from the increase in $f^{\mathcal{L}}_{env,k}$ through the third reward term (30d). Consequently, this discourages any reference contact force that produces work, conditioning the agent to adhere to the requirement outlined in the stability proof in Appendix A.

By combining these four terms, we create the comprehensive reward function (30a) that guides the robot towards desired behaviors in different scenarios.

### B. RL methodology

Given the adeptness of the A3C algorithm in addressing deep learning-supported RL challenges [21], we have chosen it to implement the automatic environment updating module in our control solution. This algorithm approximates both the policy $\pi(a|s;\theta_\pi)$ and the value function $V_\pi(s_k;\theta_v)$ by leveraging parallel agents interacting with separate copies of the environment. In the chosen implementation variant, instead of using two artificial neural networks, both functions are approximated by a single convolutional neural network, where the learning parameters $\theta_\pi$ and $\theta_v$ are partially shared. Consequently, for training the unique network we minimize a global loss function obtained from the sum of three terms:

$$L_k(\theta_\pi,\theta_v) = \sum_{i=1}^{3} \hat{L}_{i,k}; \tag{31a}$$

$$\hat{L}_{1,k}(\theta_\pi,\theta_v) = -\log\pi(a_k|s_k;\theta_\pi)(R_k - V(s_k;\theta_v)); \tag{31b}$$

$$\hat{L}_{2,k}(\theta_v) = \lambda_v(R_k - V(s_k;\theta_v))^2; \tag{31c}$$

$$\hat{L}_{3,k}(\theta_\pi) = \lambda_\beta H(\pi(a_k|s_k;\theta_\pi)). \tag{31d}$$

Here, $\lambda_v$ and $\lambda_\beta$ are hyperparameters used to scale the importance of the value loss (31c) and the entropy loss (31d) terms, respectively. The single loss functions are specified in the following list.

- The policy loss term (31b) is derived from the unbiased estimate of the expected return $\mathbb{E}[R_k]$ [21]. Therefore, minimizing this loss translates to maximizing $\mathbb{E}[R_k]$. Subtracting $V(s_k;\theta_v)$ from $R_k$ helps to lower the variance of the estimator [30].
- The value loss term (31c) aims to improve the return prediction capabilities of the value function estimator $V(s_k;\theta_v)$. This estimator learns the return associated with the state $s_k$ following the current policy $\pi$. Thus, the difference $R_k - V(s_k;\theta_v)$ represents the advantage of taking a certain generic action compared to the one suggested by the current policy [20].
- The entropy loss term (31d) is optional but aids in enhancing exploration and prevents premature convergence to a local minimum.

To update the shared common parameters $\theta_\pi$ and $\theta_v$ using the computed deltas $\Delta\theta_\pi$ and $\Delta\theta_v$ from each independent agent, we employ the RMSProp algorithm [31]. The update is performed according to the following equations:

$$\begin{aligned} g_\pi &\leftarrow \lambda_\alpha g_\pi + (1-\lambda_\alpha)\Delta\theta_\pi{}^2; \quad \theta_\pi \leftarrow \theta_\pi - \lambda_\eta \frac{\Delta\theta_\pi}{\sqrt{g_\pi + \lambda_\epsilon}}; \\ g_v &\leftarrow \lambda_\alpha g_v + (1-\lambda_\alpha)\Delta\theta_v{}^2; \quad \theta_v \leftarrow \theta_v - \lambda_\eta \frac{\Delta\theta_v}{\sqrt{g_v + \lambda_\epsilon}}, \end{aligned} \tag{32}$$

where $\lambda_\alpha$ is the decay factor, $\lambda_\eta$ is the learning rate, and $\lambda_\epsilon$ is a hyperparameter chosen to stabilize square root computation in denominator of RMSProp update. Excessively large computed deltas can have a detrimental effect on the learning process. To mitigate this issue, we apply a clipping operation on $\Delta\theta$ after a specific limit denoted by $\lambda_\zeta$. This ensures that the updates to the parameter values remain within a reasonable range.

### C. Hyperparameters tuning

To effectively employ the A3C algorithm, the identification of an appropriate set of hyperparameters is crucial. We denote this set as

$$\mathcal{H} = \begin{Bmatrix} \lambda_\eta & \lambda_\beta & n & \lambda_\epsilon & \lambda_\zeta & \lambda_\gamma & \lambda_v & \lambda_\alpha \end{Bmatrix}. \tag{33}$$

To tailor this set to our specific problem, we assess the performance reached by the algorithm at the end of the training. We use the mean reward $r_k$ averaged over the last $N$ training episodes as the fitness function. With a training size of $T$ episodes, the fitness function is defined as:

$$F_\lambda = \frac{1}{N}\sum_{k=T-N}^{T} r_k. \tag{34}$$

To maximize this function, a gradient-free approach is necessary. Among the possible choices, we opted for a genetic algorithm, a well-established methodology widely employed for similar problems [32], [33].

## V. Experiment setup

In this section, we provide details on the practical implementation of the proposed A3CQP controller and present the setup for the experiments carried out to assess its performance. In the following paragraphs, we will elaborate on the manipulator in use, the sensors and tools employed, and provide specific information about the algorithm parameters.

### A. Hardware setup

This controller has been deployed and tested on a Franka EMIKA Panda robot. Two different force and torque sensing methods are used to distinguish between the operator's interactions with the last link of the robot and contact of the end effector with the workspace. An ATI mini45 F/T (force and torque) sensor is mounted between the last link of the robot and its end effector to specifically detect any contact

**TABLE I:** QP control parameters

| Parameter | Value |
|---|---|
| $c_p$ | 3 |
| $c_v$ | 5 |
| $k_p$ | 150 |
| $k_\theta$ | 20 |
| $k_q$ | 10 |
| $\Lambda_d$ | 5 |
| $C_d$ | 5 |
| $\epsilon$ | $1 \times 10^{-4}$ |
| $\mu$ | 0.4 |

**TABLE II:** State limits

| Limit | Value |
|---|---|
| $\bar{e}_x^{\mathcal{L}}$ | 1 $m$ |
| $\bar{f}_{env}^{\mathcal{L}}$ | 30 $N$ |
| $\bar{f}_{ope}^{\mathcal{L}}$ | 15 $N$ |
| $\bar{f}_d^{\mathcal{L}}$ | 20 $N$ |

**TABLE III:** Reward parameters

| Parameter | Value |
|---|---|
| $\alpha_1$ | 0.5 |
| $\alpha_2$ | 20 |
| $\alpha_3$ | 2 |
| $\alpha_4$ | 1 |

with the workpiece or worksurface. This sensor provides the contact force $\mathbf{f}_{env,k}^{\mathcal{L}}$, already oriented in the local frame $\mathcal{L}$. During collaborative tasks, it is crucial for the operator not to touch the robot below the F/T sensor to prevent the misclassification of his interaction force as the environmental contact force. On the other hand, torque sensors embedded in each joint of the robot measure the external torque $\boldsymbol{\tau}_s$. The total external force applied at the end effector is then computed as $\mathbf{f}_{ext,k} = \mathbf{J}_k^{T\dagger}\boldsymbol{\tau}_s = \mathbf{f}_{env,k} + \mathbf{f}_{ope,k}$. By subtracting the contribution measured by the installed F/T sensor, we can isolate and determine the operator's interaction force alone.
The first experiment entails a collaborative peg-in-hole assembly. A 20 mm diameter peg is directly connected to the F/T sensor, while a 20.5 mm diameter hole is securely clamped to a known position in the worktable using a bench vise. This setup is depicted in Figure 3a. The second experiment centers around collaborative wooden board polishing. For this purpose, we design a flange to connect an Einhell drill to the F/T sensor. The drill is equipped with a polishing disc, and we control its motor speed using an Arduino[1] controller, as shown in Figure 3b.

### *B. Software implementation*

The QP controller operates at a frequency of 1 kHz, is integrated with the ROS framework, and is based on the Franka Control Interface[2]. The control parameters of the QP have been carefully tuned to achieve a reactive behavior, allowing the robot to track the desired trajectory accurately with smooth control torque profiles and gentle movements. The final values of these control parameters are described in Table I. The wrench limits are defined as $\pm$ $20N$ for the forces and $\pm 5$ $Nm$ for the torques. The position, velocity and acceleration boundaries are directly retrieved by the robot specifications. The adaptation module has been implemented as a standalone Python ROS node, running at a frequency of 100 Hz. The elements of the normalized input state $\tilde{s}_k$ are scaled to fall within the range of $[0, 1]$ before being fed into the neural network. This normalization enhances learning stability and is also applied when processing these elements and the desired contact force $f_d^{\mathcal{L}}$ in the reward

[1]https://www.arduino.cc
[2]https://frankaemika.github.io/docs

**TABLE IV:** A3C hyperparameters

| Hyperparameter | Value |
|---|---|
| $\lambda_\eta$ (Learning Rate) | $4.25339846 \times 10^{-6}$ |
| $\lambda_\beta$ (Entropy Loss Term Weight) | $3.371768978 \times 10^{-4}$ |
| $n$ (Number of Steps) | 4 |
| $\lambda_\epsilon$ (RMSProp Parameter) | $3.938214948 \times 10^{-5}$ |
| $\lambda_\zeta$ (Clipping Threshold) | 4.24498881 |
| $\lambda_\gamma$ (Discount Coefficient) | 0.99 |
| $\lambda_v$ (Value Loss Term Weight) | 0.5 |
| $\lambda_\alpha$ (RMSProp Decay Factor) | 0.99 |

**TABLE V:** Genetic Algorithm Settings

| Setting | Value |
|---|---|
| Number of Generations | 50 |
| Number of Solutions to be Selected as Parents | 4 |
| Number of Solutions within the Population | 8 |
| Number of Genes in the Solution/Chromosome | 5 |
| Parent Selection Type | Steady-State |
| Number of Parents to Keep in the Next Population | 1 |
| Type of Crossover Operation | Single Point |
| Mutation Type | Random |
| Percentage of Genes to Mutate | 10 |

function. During the normalization process, each element is divided by its empirically determined upper bound, which is set at reasonably high values to prevent excessive values under typical conditions. These parameters are listed in Table II. The weights of the reward function have been selected to establish a hierarchy among the objectives of the agent. Details of these weights can be found in Table III. The rate scaling parameters have been set to $\sigma_w = 6$ and $\sigma_f = 10$ in order to achieve task transitions from complete deactivation to complete activation within 1 or 2 seconds. The A3C algorithm has been implemented using the RL library Stable-Baselines3[3]. The hyperparameters of the algorithm, resulting from the tuning procedure, are summarized in Table IV. The genetic algorithm used for tuning the RL hyperparameters has been implemented using the library pygad[4]. The specific settings applied in this implementation are presented in Table V. The training of the A3C algorithm has been performed in a virtual Gym[5] environment. The robot dynamics are simplified by modeling them as a one-degree-of-freedom point mass system. In this system, we omit the QP controller for the sake of simplicity. The control force applied is a weighted sum of several components: a PD position control contribution for inverse kinematic tracking, an admittance control force designed to achieve desired virtual dynamics, and the desired contact force. The dynamic equation for the simplified system is as follows:

$$\begin{aligned}\Lambda\ddot{x}_k = f_{ext,k}^{\mathcal{L}} + w_1\Lambda(K_p e_{x,k} - K_v\dot{x}_k + \ddot{x}_{pd}) + \\ w_2\left(\frac{\Lambda}{\Lambda_d} - 1\right) f_{ext,k}^{\mathcal{L}} - w_2 C_d\dot{x} + w_3 f_d^{\mathcal{L}},\end{aligned} \tag{35}$$

with $\Lambda = 10$.

[3]https://stable-baselines3.readthedocs.io/en/master/modules/a2c.html
[4]https://pygad.readthedocs.io/en/latest/
[5]https://www.gymlibrary.dev/index.html

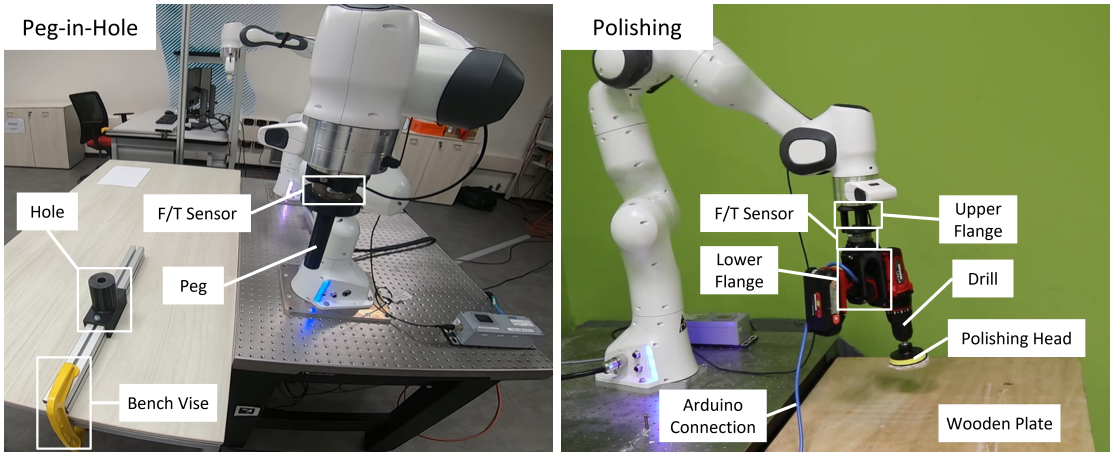


**(a)** Setup for the collaborative peg-in-hole assembly experiment. **(b)** Setup for the collaborative polishing experiment.

**Fig. 3:** The experimental setups. It is important to note that the operator must interact with the robot above the F/T sensor to prevent the misclassification of his interaction force $\mathbf{f}_{ope}$ as the environment contact force $\mathbf{f}_{env}$.

## VI. Results

In this section, we begin by presenting and discussing the results of training the A3C algorithm. Subsequently, we provide an overview of the two experimental tests that were carried out to validate the entire pipeline. The first experiment centers around a collaborative peg-in-hole assembly, while the second one is focused on collaboratively polishing a wooden board. Both of these experiments are showcased in the accompanying video[6] associated with this paper.

### A. Training results

In order to train the A3C algorithm, which is utilized by the adaptation module to dynamically adjust QP priorities and select the desired contact force in real-time, we conducted simulations over a total of $1e6$ time steps using four parallel virtual environments. We followed the approach described in the algorithm version mentioned in [22], where the four parallel agents each complete their own segments of experience before updating the global network. The learning process took approximately one hour. To thoroughly assess the learning performance of the algorithm, we conducted 20 repetitions of the process to gather data on the behavior of the policy loss $\hat{L}_{1,k}$ and value loss $\hat{L}_{2,k}$ during training. These trends are depicted in Figure 4, where the means are averaged across all four agents, and the interquartile range represents the spread between the 25th and 75th percentiles. The policy loss $\hat{L}_{1,k}$, as defined in equation (31b), increases as the expected return $\mathbb{E}[R_k]$ of the agent's choices increases. On the other hand, the value loss $\hat{L}_{2,k}$, expressed in equation (31c), decreases as the estimator $V$ progressively fits the return $R_k$ more accurately.

Figure 5 presents the policy optimized by the algorithm at the end of the training. Each subplot visualizes one component of the action $a_k$ within the state space $S_k$. The combination of these components describes the behavior of the adaptation module in various situations. The visual representation effectively divides $S_k$ into distinct colored regions based on the

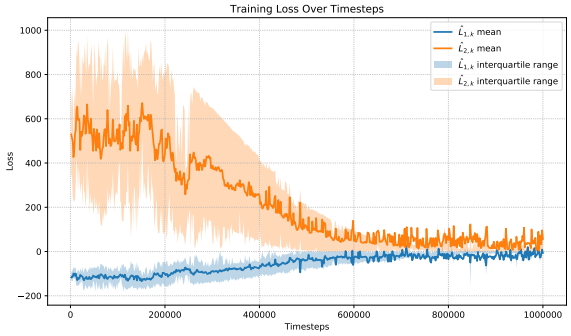


**Fig. 4:** Visual representation depicts the trends of policy loss $\hat{L}_{1,k}$ and value loss $\hat{L}_{2,k}$ over $1e6$ time steps in the training process. This data is aggregated from 20 training processes, presenting the mean and interquartile range for clarity and comprehensive insight.

decided prioritization. In the edge characterized by a large operator force $f^{\mathcal{L}}_{ope}$ and a minimal contact force with the fixed environment $f^{\mathcal{L}}_{env}$, the AC task priority $w^{\mathcal{L}}_2$ tends to rise, while the priorities of other tasks decrease. A higher position error $e^{\mathcal{L}}_x$ contributes to accelerating the activation of the AC task. This region proves to be the sole area where the AC task is strongly encouraged, yielding positive results and confirming that the relationship between this task and the operator presence has been learned. Conversely, in the opposing edge where $f^{\mathcal{L}}_{ope}$ is low and $f^{\mathcal{L}}_{env}$ is high, the priority for the FC control task and the value of the desired contact force $f^{\mathcal{L}}_d$ increase. Thus, the combined effect of the third (30d) and fourth (30e) reward terms manifests in linking the dynamics of these two variables. This is the region of the state space $S_k$ allocated by the autonomous agent to the interaction with the workspace. Lastly, the IK task priority increases more significantly when both $f^{\mathcal{L}}_{ope}$ and $f^{\mathcal{L}}_{env}$ are absent. However, it can also rise in the presence of $f^{\mathcal{L}}_{env}$ if the positional error $e^{\mathcal{L}}_x$ is substantial. This implies that activities related to reaching a target are prioritized when the manipulator is not interacting with the environment, but the robot can cease interaction

[6]https://youtu.be/ykRe4dzah6o

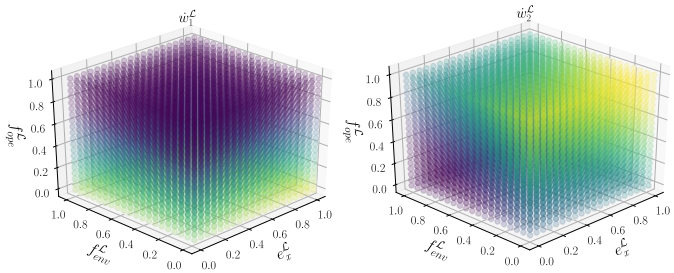

**(a)** Visualization of $\dot{w}^{\mathcal{L}}_{1,k}$ reveals that high positive values correspond to large positional errors $e^{\mathcal{L}}_{x,k}$ and low operator and environment forces $f^{\mathcal{L}}_{ope,k}, f^{\mathcal{L}}_{env,k}$.

**(b)** Visualization of $\dot{w}^{\mathcal{L}}_{2,k}$ displays high positive values when there are large positional errors and operator forces $e^{\mathcal{L}}_{x,k}, f^{\mathcal{L}}_{ope,k}$, and low environmental forces $f^{\mathcal{L}}_{env,k}$.

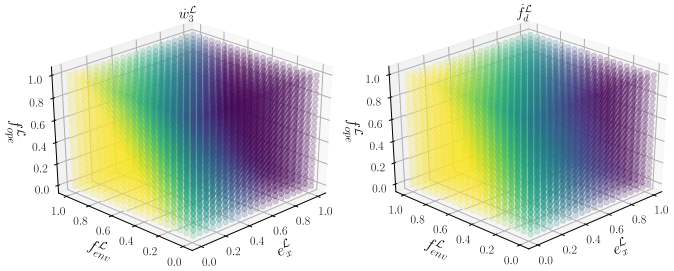

**(c)** Visualization of $\dot{w}^{\mathcal{L}}_{3,k}$ demonstrates high positive values for significant environmental forces $f^{\mathcal{L}}_{env,k}$ and low positional errors and operator forces $e^{\mathcal{L}}_{x,k}, f^{\mathcal{L}}_{ope,k}$.

**(d)** Visualization of $\dot{f}^{\mathcal{L}}_{d,k}$ demonstrates high positive values for significant environmental forces $f^{\mathcal{L}}_{env,k}$ and low positional errors and operator forces $e^{\mathcal{L}}_{x,k}, f^{\mathcal{L}}_{ope,k}$.

**Fig. 5:** Plot of the four action components $a_k = \{\dot{w}^{\mathcal{L}}_{1,k} \quad \dot{w}^{\mathcal{L}}_{2,k} \quad \dot{w}^{\mathcal{L}}_{3,k} \quad \dot{f}^{\mathcal{L}}_{d,k}\}$ according to the three component of the state $s_k = \{e^{\mathcal{L}}_{x,k} \quad f^{\mathcal{L}}_{env,k} \quad f^{\mathcal{L}}_{ope,k}\}$. In this visualization, the color yellow indicates high positive rate of change values near 1, while the dark blue color represents high negative rate of change values near -1.

with the workspace if the target changes. Remarkably, in the learned behavior, the desired contact force $f^{\mathcal{L}}_d$ along a Cartesian direction can only increase when the end-effector is already in contact and the associated Cartesian velocity is null. Therefore, the contact force cannot perform positive work while the manipulator is approaching the desired target. Starting from a contact condition, when the target changes, the transition from the FC task to the IK task begins. During this continuous transition, the manipulator moves in a direction opposite to the reference contact force, generating negative work that does not compromise the stability of the system.

### *B. Experimental validation*

The performance of the proposed A3CQP controller has been evaluated in two collaborative industrial scenarios: a peg-in-hole assembly and the polishing of a wooden plate. These comprehensive jobs engage all the functionalities the controller can manage. They involve stages where the robot needs to precisely follow a predefined Cartesian position $\mathbf{x}_{d,k}$ generated by a trajectory planner, phases where the robot must establish a robust physical connection with the workpiece or the worksurface to accomplish the task effectively, and intervals where the operator directly interacts with the robot to physically guide its movements in the workspace.

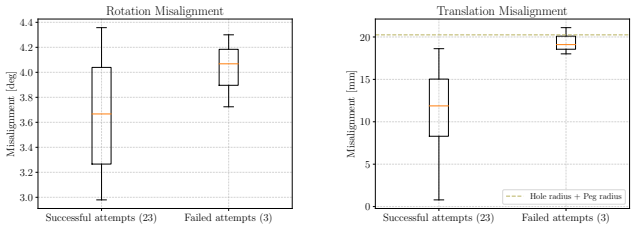


**(a)** **(b)**

**Fig. 6:** Box plots depict the stochastic distribution of translation 6b and rotation 6a misalignments in the peg-in-hole experiment. Above the dashed line, the translation misalignment is substantial, causing the peg to make contact with the hole structure outside its edges. Notably, failed tests show values of translation misalignment around this line, resulting in minimal contact with the hole edge. Despite rotation misalignments exceeding the average in these cases, the controller could effectively manage them if accompanied by lower translation misalignments.

*1) Peg-in-hole experiment:* A total of 26 peg insertions were executed throughout this test. Figure 7 illustrates the operation of the adaptation module and depicts the dynamics of peg-hole misalignment for three successively insertions. For comprehensive experiment results, please consult Table VI. The robot starts from an initial *home* position, and the

**TABLE VI:** Peg-in-Hole Experiment Results

| | | |
|---|---|---|
| Success | Total attempts | 26 |
| | Successful attempts | 23 |
| | | 89% |
| Speed | Insertion time | $8.21 \pm 0.24$ s |
| Robustness | Rotation Misalignment | $3.66 \pm 0.45$ deg |
| | Translation Misalignment | $12.30 \pm 4.24$ mm |
| Equipment | Peg | $\varnothing$ 20.0 mm |
| | Hole | $\varnothing$ 20.5 mm |

controller guides it to an *approach* pose, aligning with the hole. When the alignment is achieved within a specified tolerance, the reference position $\mathbf{x}_{d,k}$ is adjusted again to begin the peg insertion going to the *contact* pose. Owing to the relatively lenient alignment tolerances enforced during the IK task phase, the peg typically initially enters into the FC task along the z-axis while in contact with the external hole border. These moments correspond to time instants at 7.7 s, 41.0 s, and 96.9 s, during which the misalignment error primarily manifests as translation error. These moments are depicted in snapshot (A) of Figure 7. The transition from IK to the FC task along the z-axis is triggered by the detection of an initial minor environmental force. This detection prompts the adaptation module to simultaneously increase both $w^{\mathcal{L},z}_3$ and $f^{\mathcal{L},z}_d$ while reducing $w^{\mathcal{L},z}_1$. These dynamics are visually represented in Figures 5c, 5d, and 5a. This phase results in a sudden, slight deviation in $e^{\mathcal{L},z}_x$ as the system ceases to track the Cartesian reference in that particular direction. Notably, following the initial minor force $f^{\mathcal{L},z}_{env}$ measured after the first contact, there is a significant increase in $f^{\mathcal{L},z}_{env}$ to match the desired $f^{\mathcal{L},z}_d$. This leads to noticeable steps in the plot. At this point, the synergy

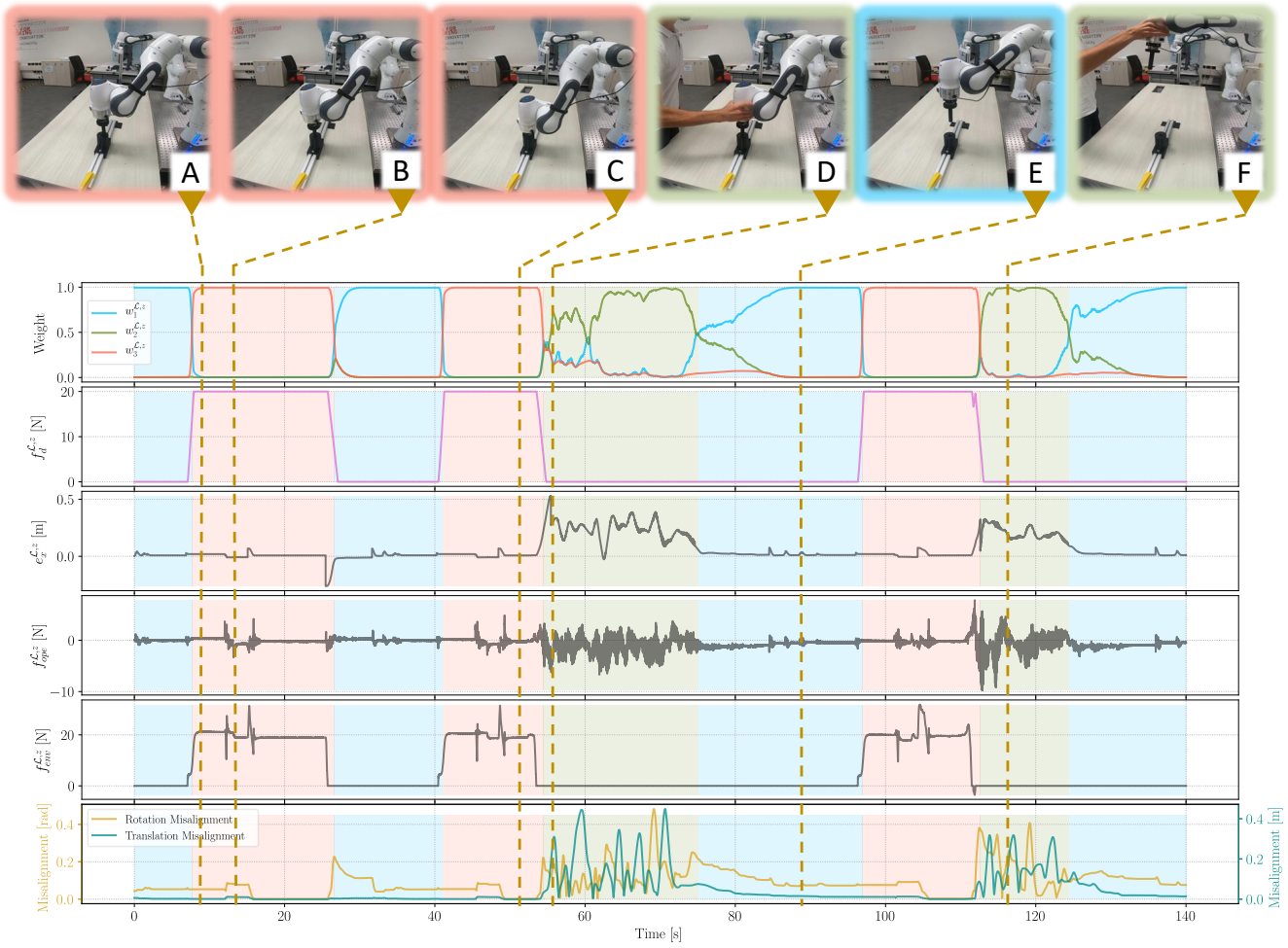


**Fig. 7:** Peg-in-hole experiment results. The top two plots display the action $a^z$ determined by the adaptation module in the z Cartesian direction during the peg-in-hole experiment. The latter is based on the input state $s^z$, which is depicted in the subsequent three plots. The bottom plot illustrates the dynamics of the peg-hole translation and rotation misalignment. Color-coded patches are employed to highlight the primary controller task: blue signifies the IK task phases, red corresponds to the FC task phases, and green represents the AC task phases. At the upper portion of the image, six snapshots obtained during the experiment are situated. The first three snapshots capture the different phases of the FC task. In (A), the initial contact of the peg with the external hole border is visible. Moving on to (B), it illustrates the peg successfully intercepting the hole while maintaining contact. Finally, (C) displays the peg being inserted into the hole. Snapshot (D) documents the transition from the FC task to the AC task as the operator manually disengages the peg-hole assembly. After the interaction with the operator in (E), the robot returns to its "approach" pose. Snapshot (F) represents a moment of inspection captured during the final collaborative interaction.

between the FC task in the z-direction, exerting downward pressure on the peg, and the IK task in the x and y directions, which continue to guide the peg toward the desired position in the x-y plane, allows the peg to slip into the hole when it intercepts it during the approach maneuvers. These maneuvers are accompanied by force shocks measured in both $f_{env}^{\mathcal{L},z}$ and $f_{ope}^{\mathcal{L},z}$ but do not result in any perceivable change in the task weights, indicating that the controller dynamics remain robust against these disturbances. When the peg intercepts the hole at time instants 12.2 s, 45.5 s, and 101.5 s, there is an increase in misalignment due to the rotation caused by the reaction forces of the hole walls. This specific moment is observable in snapshot (B) of Figure 7. In this situation, the downward force exerted by the FC task guides the peg within the hole. As a result, at time instants 15.9 s, 49.3 s, and 105.9 s, the misalignment is nullified, demonstrating the successful insertion of the peg. This moment is captured in snapshot (C). The large $e_x^{\mathcal{L},z}$ value registered at 26.2 s is a result of the robot return to the *home* position after the initial insertion. During the subsequent two insertions, the operator manually disengages the peg from the hole at 54.4 s and 112.6 s. This leads to a noticeable presence of a consistent operator force $f_{ope}^{\mathcal{L},z}$, causing a subsequent increase in $w_2^{\mathcal{L},z}$ in line with the expected agent behavior represented in Figure 5b. This transition, represented by snapshot (D), results in a sharp increase in misalignment and position error $e_x^{\mathcal{L},z}$ since the reference $\mathbf{x}_d$ and the hole placement remain unchanged. Following the decrease in $f_{ope}^{\mathcal{L},z}$, $w_1^{\mathcal{L},z}$, driven by the objective to reduce $e_x^{\mathcal{L},z}$, takes the lead again at time instants 75.1 s and 124.4 s, allowing the manipulator to smoothly return to the

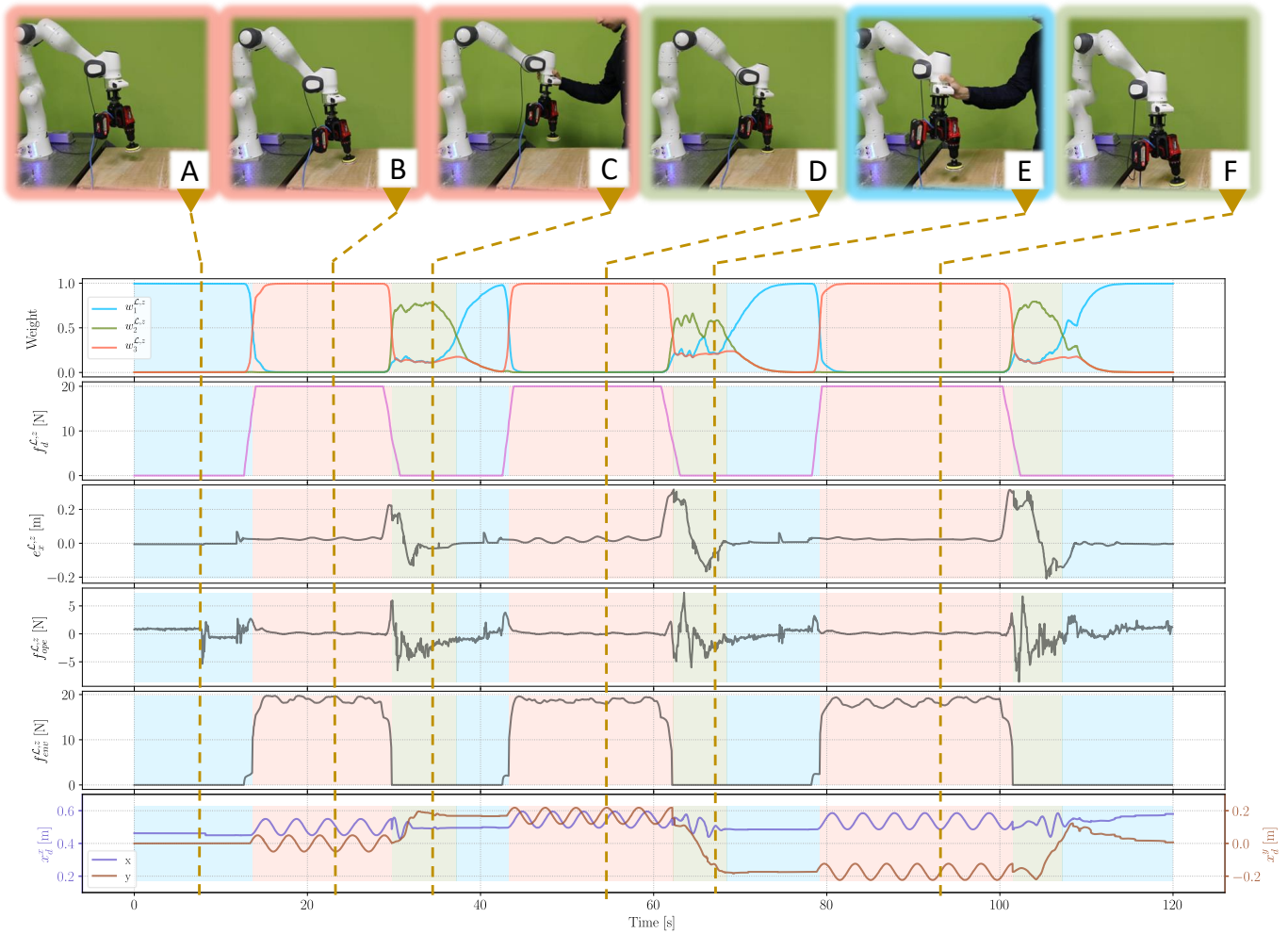


**Fig. 8:** Polishing experiment results. The top two plots showcase the action $a^z$ determined by the adaptation module in the z Cartesian direction throughout the polishing experiment. This action is based on the input state $s^z$, visualized in the following three plots. The bottom plot illustrates the behavior of the desired reference position in the Cartesian x-y plane, specifically $x_d^x$ and $x_d^y$. These reference positions describe circles whose centers are modified in response to the operator's intervention. To highlight the prevailing controller task at any given time, color-coded patches are utilized. Just as before, the color blue denotes the IK task phases, red represents the FC task phases, and green corresponds to the AC task phases. At the upper portion of the image, six snapshots obtained during the experiment are situated. The first snapshot (A) portrays the robot in its initial *rest* position before making contact with the plate. The second snapshot (B) illustrates the first phase of polishing, with the robot concentrating on the central part of the plate. Following some moments of work, (C) shows the operator shifting the end effector to the right, with the robot continuing its work in position (D). In (E), the operator opts to move the robot to the left, allowing it to complete the polishing on that side of the plate (F).

*home* position. This moment is depicted in snapshot (E).

As illustrated in Table VI, the adoption of the proposed A3CQP controller in the selected peg-in-hole assembly enables successful and autonomous task execution. This effectiveness persists even in the face of uncertainties in the hole position, thanks to the controller adept utilization of the FC task, which effectively eliminates peg-hole misalignment. As demonstrated in Figure 6, the controller reliably handles significant misalignment errors and exhibits reduced reliability only when the peg center point contacts the hole structure outside its edges. Controllers designed specifically for this task, such as [34], utilize a contact model to address alignment uncertainties and can handle stricter coupling clearances. However, these controllers exhibit effectiveness within limited initial misalignment ranges, typically within 1 mm. On the other hand, other task-specific learning-based controllers, such as those discussed in [35] and [36], which operate with clearances and initial misalignments closer to our setup, exhibit slower insertion times, approximately 15 s and 30 s as reported in the respective papers. In contrast, our proposed general approach can accommodates multiple tasks in series, allowing uninterrupted execution. An other essential feature is its adaptability to operator intervention at any point during the operation. The controller smoothly transitions to accommodate the operator's commands, even when the robot is already in contact with the workpiece.

*2) Polishing experiment:* To assess the flexibility of the proposed controller, a polishing job was conducted as the second experiment. The actions of the adaptation module and the behavior of the desired reference position are illustrated

in Figure 8. The robot starts from an initial *rest* position, with the tool not yet in contact with the wooden plate intended for polishing. After a brief interval in which the system velocity is maintained null, the A3CQP controller directs the robot to make contact with the work surface, moving towards the *polishing* pose. There, the planar translation components of the desired Cartesian position $\mathbf{x}_d$, specifically $x_d^x$ and $x_d^y$, are adjusted to trace a circular trajectory on the work surface. Simultaneously, the Arduino controller activates the drill motor to spin at 50 rpm. The robot makes contact with the wooden plate three times to polish specific areas until the operator intervenes to change the working zone. As shown earlier, when the agent senses the initial contact force with the plate, it triggers the FC task in the z Cartesian direction. This results in three distinct steps in the environment contact force $f_{env}^{\mathcal{L},z}$ at time instants of 13.6 s, 43.3 s, and 79.2 s. In this phase, the desired reference position is continuously adjusted to follow a circular trajectory, corresponding to sinusoidal references for the coordinates $x_d^x$ and $x_d^y$. Unlike before, due to the periodic motion in the x-y plane, the $f_{env}^{\mathcal{L},z}$ no longer remains mainly flat during the contact phase. Instead, it exhibits sinusoidal oscillations, which are also visible in the position error $e_x^{\mathcal{L},z}$ and introduce measurement noise in the operator interaction force $f_{ope}^{\mathcal{L},z}$. However, despite these movements, the manipulator, leveraging the FC task, maintains the polishing head aligned with the plate and exerts the necessary force for the polishing task. When the operator intervenes, indicated by the sudden rise in $f_{ope}^{\mathcal{L},z}$ at time instants 29.7 s, 62.2 s, and 101.5 s, the transition to the AC task phase occurs. In these moments, the operator grabs the manipulator end effector, physically guides it to a new working region, and then releases it. During this interval, the planar references $x_d^x$ and $x_d^y$ change to align with the new positions the robot assumes under the operator's guidance. Once released, at time instants 37.2 s, 68.5 s, and 107.3 s, the robot reactivates the IK task to stabilize the last position taught by the operator. After a brief period of maintaining this position at zero velocity, the robot is prepared to return to the wooden plate and recommence the polishing activity from the new position. The snapshots of the experiment, as illustrated in Figure 8, document the various phases of the polishing process. At first, the robot concentrates on the central area of the plate, as captured in (B). It is then repositioned to the right by the operator, depicted in snapshots (C) and (D). Subsequently, the robot is shifted to the left, as seen in snapshots (E) and (F), where it concludes the polishing task.

In conclusion, the presented A3CQP controller is not limited to a single category of jobs. Instead, it equips the robot with the flexibility to adapt to a diverse range of activities. These activities may require autonomous tasks involving interaction with the environment, and the operator is free to step in and collaborate with the robot. In this case, the operator indicates which areas of the plate require attention.

## VII. Conclusion

In this work, we have devised an innovative A3CQP controller aimed at enhancing the robot adaptability when tackling complex, unstructured tasks. This controller is grounded in a non-strict hierarchical Quadratic Programming algorithm, seamlessly incorporating both motion and interaction capabilities. It ensures that control inputs remain stable, consistent, and predictable while adhering to specific constraints. What distinguishes this controller is its ability to dynamically and autonomously adjust task priorities. It employs a Reinforcement Learning-based adaptation module, which leverages the Asynchronous Advantage Actor-Critic algorithm. This approach ensures swift convergence and steady training within the continuous action and observation spaces. This adaptation module plays a pivotal role in endowing the robot with the ability to learn from its interactions with the environment. It empowers the robot to smoothly transition between three essential tasks: the Cartesian Inverse Kinematic Task, Cartesian Admittance Control Task, and Cartesian Force Control Task. These tasks span a wide range of behaviors, from precise position tracking for manipulation to exerting specific forces during physical interactions and following operator guidance for co-manipulation. To assess the validity of our proposed solution, we conducted a series of experiments. These tests encompassed both collaborative peg-in-hole assembly and the cooperative polishing of a wooden plate, employing the Franka Emika Panda robot. The outcomes of these evaluations demonstrate the robot adeptness in combining a variety of tasks to fulfill the specific needs of different job phases. These activities necessitate autonomous operations involving interactions with the environment, and the operator retains the flexibility to intervene and collaborate with the robot as needed.

## Appendix

To demonstrate the stability of the optimal control problem outlined in (24), it is essential to derive the analytical expressions for the two optimization variables $\ddot{\mathbf{q}}_k^*$ and $\mathbf{f}_k^*$. To achieve this, we utilize the Karush-Kuhn-Tucker (KKT) conditions [37], and apply them to the associated sub-problems. For the initial sub-problem (24a) pertaining to $\ddot{\mathbf{q}}_k^*$, the KKT conditions are as follows:

$$\begin{aligned}&(1+\epsilon)\mathbf{J}_k^T\mathbf{w}_1\mathbf{J}_k\ddot{\mathbf{q}}_k^* - \mathbf{J}_k^T\mathbf{w}_1\left(\mathbf{K}_p\mathbf{e}_{x,k} - \mathbf{K}_v\dot{\mathbf{x}} - \dot{\mathbf{J}}_k\dot{\mathbf{q}}_k\right) - \\ &\mathbf{J}_k^T\epsilon\mathbf{w}_1\mathbf{J}_k\left(k_q\mathbf{e}_{q,k} - 2\sqrt{k_q}\dot{\mathbf{q}}_k\right) + \bar{\boldsymbol{\mu}}_q^T + \underline{\boldsymbol{\mu}}_q^T = 0;\end{aligned} \tag{36a}$$

$$\ddot{\mathbf{q}}_k^* - \bar{\ddot{\mathbf{q}}} \leq 0; \quad \bar{\boldsymbol{\mu}}_q^T\left(\ddot{\mathbf{q}}_k^* - \bar{\ddot{\mathbf{q}}}\right) = 0; \quad \bar{\boldsymbol{\mu}}_q^T \geq 0. \tag{36b}$$

$$\ddot{\mathbf{q}}_k^* - \underline{\ddot{\mathbf{q}}} \geq 0; \quad \underline{\boldsymbol{\mu}}_q^T\left(\ddot{\mathbf{q}}_k^* - \underline{\ddot{\mathbf{q}}}\right) = 0; \quad \underline{\boldsymbol{\mu}}_q^T \leq 0. \tag{36c}$$

The KKT conditions associated to the second sub-problem (24b) concerning $\mathbf{f}_k^*$ are:

$$\begin{aligned}&[\mathbf{w}_2 + \mathbf{w}_3]\mathbf{f}_k^* - \mathbf{w}_2\left([\boldsymbol{\Lambda}_k\boldsymbol{\Lambda}_d^{-1}] - \mathbf{I}_{6\times6}\right)\mathbf{f}_{ext,k} + \\ &\mathbf{w}_2(\mathbf{C}_d\mathbf{J}_k + \boldsymbol{\Lambda}_k\dot{\mathbf{J}}_k)\dot{\mathbf{q}} - \mathbf{w}_3\mathbf{f}_{ctc,k} + \bar{\boldsymbol{\mu}}_f^T + \underline{\boldsymbol{\mu}}_f^T = 0;\end{aligned} \tag{37a}$$

$$\mathbf{f}_k^* - \bar{\mathbf{f}} \leq 0; \quad \bar{\boldsymbol{\mu}}_f^T\left(\mathbf{f}_k^* - \bar{\mathbf{f}}\right) = 0; \quad \bar{\boldsymbol{\mu}}_f^T \geq 0. \tag{37b}$$

$$\mathbf{f}_k^* - \underline{\mathbf{f}} \geq 0; \quad \underline{\boldsymbol{\mu}}_f^T\left(\mathbf{f}_k^* - \underline{\mathbf{f}}\right) = 0; \quad \underline{\boldsymbol{\mu}}_f^T \leq 0. \tag{37c}$$

The stability of the presented QP controller can be discussed using Lyapunov theory, with the following positive definite candidate function:

$$V = \frac{1}{2}\dot{\mathbf{x}}_k^T\dot{\mathbf{x}}_k + \frac{1}{2(1+\epsilon)}\mathbf{e}_{x,k}^T\mathbf{K}_p\mathbf{e}_{x,k} + \frac{\epsilon k_q}{2(1+\epsilon)}\mathbf{e}_{q,k}^T\mathbf{J}_k^T\mathbf{J}_k\mathbf{e}_{q,k}; \tag{38}$$

The associated time derivative is

$$\begin{aligned}\dot{V} = \dot{\mathbf{x}}_k^T\ddot{\mathbf{x}}_k + \frac{1}{1+\epsilon}\dot{\mathbf{e}}_{x,k}^T\mathbf{K}_p\mathbf{e}_{x,k} + \\ \frac{\epsilon k_q}{1+\epsilon}\dot{\mathbf{e}}_{q,k}^T\mathbf{J}_k^T\mathbf{J}_k\mathbf{e}_{q,k} + \frac{\epsilon k_q}{1+\epsilon}\mathbf{e}_{q,k}^T\mathbf{J}_k^T\dot{\mathbf{J}}_k\mathbf{e}_{q,k}.\end{aligned} \tag{39}$$

This equation can be rewritten by explicating the acceleration $\ddot{\mathbf{x}}_k$ using the Cartesian dynamics (12), where we incorporate the analytical expression of $\boldsymbol{\tau}$ as given in (4). In this context, we substitute the optimal variables $\ddot{\mathbf{q}}_k^*$ and $\mathbf{f}_k^*$ with their analytical expressions derived from the KKT conditions (36), (37). The feedback joint acceleration $\ddot{\mathbf{q}}_{pd,k}$, as defined in (5), does not affect system stability when the gains are appropriately tuned [24]. Consequently, we opt to exclude it from consideration, leading us to the subsequent formulation for the derivative of the Lyapunov candidate:

$$\begin{aligned}\dot{V} = \frac{1}{1+\epsilon}\dot{\mathbf{x}}_k^T\left(\epsilon\dot{\mathbf{J}}_k\mathbf{J}_k^\dagger - \mathbf{K}_v - 2\epsilon\sqrt{k_q}\mathbf{I}_{6\times6}\right)\dot{\mathbf{x}}_k + \\ \frac{1}{1+\epsilon}\dot{\mathbf{x}}_k^T\mathbf{K}_p\mathbf{e}_{x,k} + \frac{\epsilon k_q}{1+\epsilon}\dot{\mathbf{q}}_k^T\mathbf{J}_k^T\mathbf{J}_k\mathbf{e}_{q,k} - \\ \frac{1}{1+\epsilon}\dot{\mathbf{q}}_k^T[\mathbf{J}_k^T\mathbf{w}_1\mathbf{J}_k]^{-1}(\bar{\boldsymbol{\mu}}_q^T + \underline{\boldsymbol{\mu}}_q^T) + \\ \frac{1}{1+\epsilon}\dot{\mathbf{e}}_{x,k}^T\mathbf{K}_p\mathbf{e}_{x,k} + \frac{\epsilon k_q}{1+\epsilon}\dot{\mathbf{e}}_{q,k}^T\mathbf{J}_k^T\mathbf{J}_k\mathbf{e}_{q,k} + \\ \frac{\epsilon k_q}{1+\epsilon}\mathbf{e}_{q,k}^T\mathbf{J}_k^T\dot{\mathbf{J}}_k\mathbf{e}_{q,k} + P_{ext} + P_{int};\end{aligned} \tag{40}$$

$$P_{ext} = \dot{\mathbf{x}}_k^T\boldsymbol{\Lambda}_k^{-1}\mathbf{f}_{ext,k}; \tag{41}$$

$$\begin{aligned}P_{int} = \dot{\mathbf{x}}_k^T\boldsymbol{\Lambda}_k^{-1}\mathbf{f}_k^* = \dot{\mathbf{x}}_k^T\mathbf{A}_k\mathbf{w}_2\left([\boldsymbol{\Lambda}_k\boldsymbol{\Lambda}_d^{-1}] - \mathbf{I}_{6\times6}\right)\mathbf{f}_{ext,k} + \\ \dot{\mathbf{x}}_k^T\mathbf{A}_k\mathbf{w}_2\left(\boldsymbol{\Lambda}_k\dot{\mathbf{J}}_k\mathbf{J}_k^\dagger - \mathbf{C}_d\right)\dot{\mathbf{x}}_k + \\ \dot{\mathbf{x}}_k^T\mathbf{A}_k\mathbf{w}_3\mathbf{f}_{ctc,k} - \dot{\mathbf{x}}^T\mathbf{A}_k(\bar{\boldsymbol{\mu}}_f^T + \underline{\boldsymbol{\mu}}_f^T);\end{aligned} \tag{42}$$

$$\mathbf{A}_k = \boldsymbol{\Lambda}_k^{-1}[\mathbf{w}_2 + \mathbf{w}_3]^{-1}. \tag{43}$$

In this context, $P_{ext}$ represents the mass-normalized external power introduced into the system due to interaction with the operator. On the other hand, $P_{int}$ indicates the mass-normalized power internally generated when either the AC or the FC tasks, or both, are active. The matrix $\mathbf{A}_k \in \mathbb{R}^{6\times6}$ is symmetric and positive definite.

In the subsequent discussion, through the application of Lemmas 1 and 2, Theorem 4 will illustrate that the expression $P_{ext}+P_{int}$, denoting the introduced and generated power, does not jeopardize the intrinsic stability of the system. Following this, by building upon the obtained result and utilizing Lemma 3, Theorem 5 will establish the overall stability of the system.

**Lemma 1.** *The damping component of the admittance force $f_{adm}$ constitutes a purely dissipative contribution, i.e.,*

$$\dot{\mathbf{x}}_k^T\mathbf{A}_k\mathbf{w}_2\left(\boldsymbol{\Lambda}_k\dot{\mathbf{J}}_k\mathbf{J}_k^\dagger - \mathbf{C}_d\right)\dot{\mathbf{x}}_k < 0. \tag{44}$$

*Proof.* $\mathbf{A}_k\mathbf{w}_2$ is a multiplication of symmetric positive definite matrices, and $\left(\boldsymbol{\Lambda}_k\dot{\mathbf{J}}_k\mathbf{J}_k^\dagger - \mathbf{C}_d\right)$ is symmetric and negative definite when $\mathbf{C}_d > \boldsymbol{\Lambda}_k\dot{\mathbf{J}}_k\mathbf{J}_k^\dagger$. □

**Lemma 2.** *The Lagrange multipliers introduced by the wrench constraints $\bar{\boldsymbol{\mu}}_f^T, \underline{\boldsymbol{\mu}}_f^T$, do not contribute to the generation of power, i.e.,*

$$-\dot{\mathbf{x}}_k^T\mathbf{A}_k(\bar{\boldsymbol{\mu}}_f^T + \underline{\boldsymbol{\mu}}_f^T) \leq 0. \tag{45}$$

*Proof.* $[\mathbf{J}_k^T\mathbf{w}_1\mathbf{J}_k]^{-1}$ is symmetric and positive definite. $\bar{\boldsymbol{\mu}}_q^T = 0, \underline{\boldsymbol{\mu}}_q^T = 0$ whenever $\ddot{\mathbf{q}}_k^*$ is far from the limits. When $\ddot{\mathbf{q}}_k^* = \bar{\ddot{\mathbf{q}}}$, the KKT conditions (36) result in $\bar{\boldsymbol{\mu}}_q^T > 0$. Additionally, with sufficiently small sampling time $\Delta t$, the constraints employed lead to $\dot{\mathbf{q}}_k > 0$ [27]. Similarly, when $\ddot{\mathbf{q}}_k^* = \underline{\ddot{\mathbf{q}}}$, $\underline{\boldsymbol{\mu}}_q^T < 0$ and $\dot{\mathbf{q}}_k < 0$. □

**Lemma 3.** *The inclusion of joint limits in the optimization problem* (24) *does not impact the stability of the system, i.e.,*

$$-\frac{1}{1+\epsilon}\dot{\mathbf{q}}_k[\mathbf{J}_k^T\mathbf{w}_1\mathbf{J}_k]^{-1}(\bar{\boldsymbol{\mu}}_q^T + \underline{\boldsymbol{\mu}}_q^T) \leq 0 \;\forall\; \dot{\mathbf{q}}_k, \bar{\boldsymbol{\mu}}_q^T, \underline{\boldsymbol{\mu}}_q^T. \tag{46}$$

*Proof.* $\bar{\boldsymbol{\mu}}_f^T = \underline{\boldsymbol{\mu}}_f^T = 0$ whenever $\mathbf{f}_k^*$ is far from the limits. At the limits, when $\mathbf{f}_k^* = \bar{\mathbf{f}}$, the KKT conditions (37) result in $\bar{\boldsymbol{\mu}}_f^T > 0$, and $\dot{\mathbf{x}}_k > 0$ if $\mathbf{f}_k^*$ is performing positive work. Equivalently, when $\mathbf{f}_k^* = \underline{\mathbf{f}}$, $\underline{\boldsymbol{\mu}}_f^T < 0$ and $\dot{\mathbf{x}}_k < 0$. □

**Theorem 4.** *The power introduced into or generated by the robot, operating according to the QP controller formalized in* (24)*, does not compromise the intrinsic stability of the system, i.e.,*

$$P_{ext} + P_{int} < 0. \tag{47}$$

*Proof.* In light of the lemmas 1 and 2, the total power can be limited as follows:

$$\begin{aligned}P_{ext} + P_{int} < \; \dot{\mathbf{x}}_k^T\tilde{\boldsymbol{\Lambda}}_k^{-1}\mathbf{f}_{ext,k} + \dot{\mathbf{x}}_k^T\mathbf{A}_k\mathbf{w}_3\mathbf{f}_{ctc,k}; \\ \tilde{\boldsymbol{\Lambda}}_k^{-1} = \boldsymbol{\Lambda}_k^{-1} + \mathbf{A}_k\mathbf{w}_2\left([\boldsymbol{\Lambda}_k\boldsymbol{\Lambda}_d^{-1}] - \mathbf{I}_{6\times6}\right).\end{aligned} \tag{48}$$

The first term of the upper bound $\dot{\mathbf{x}}_k^T\tilde{\boldsymbol{\Lambda}}_k^{-1}\mathbf{f}_{ext,k}$ represents an external disturbance with a bounded dependency on the robot state. Consequently, it does not impact the intrinsic stability of the system and can be excluded from the discussion [38]. The second term $\dot{\mathbf{x}}_k^T\mathbf{A}_k\mathbf{w}_3\mathbf{f}_{ctc,k}$ denotes the power generated by the contact force. To ensure a non-positive contribution, it is essential for the reference contact force $\mathbf{f}_{ctc,k}$ and the end effector Cartesian velocity $\dot{\mathbf{x}}_k$ not to be oriented in the same direction. This requirement leads to the necessity for the adaptation module to adapt $\mathbf{f}_{d,k}^{\mathcal{L}}$ to satisfy this condition. By adhering to this requirement, the equation (48) equals (47), thereby proving the theorem. □

**Theorem 5.** *The QP controller formalized in* (24) *is asymptotically stable, as per the positive definite and continuously differentiable Lyapunov candidate $V$ given by* (38)*.*

*Proof.* To prove the theorem, it is necessary to demonstrate that the time derivative of the Lyapunov candidate $\dot{V}$ is negative definite.

Building upon Theorem 4, we can revisit (40) by omitting the

term $P_{ext} + P_{int}$. Additionally, recognizing that $\dot{\mathbf{e}}_{x,k} = -\dot{\mathbf{x}}_k$ and $\dot{\mathbf{e}}_{q,k} = -\dot{\mathbf{q}}_k$, we can simplify the equation as follows:

$$\dot{V} = \frac{1}{1+\epsilon}\dot{\mathbf{x}}_k^T \left(\epsilon\dot{\mathbf{J}}_k\mathbf{J}_k^\dagger - \mathbf{K}_v - 2\epsilon\sqrt{k_q}\mathbf{I}_{6\times 6}\right)\dot{\mathbf{x}}_k - \frac{1}{1+\epsilon}\dot{\mathbf{q}}_k[\mathbf{J}_k^T\mathbf{w}_1\mathbf{J}_k]^{-1}(\bar{\boldsymbol{\mu}}_q^T + \underline{\boldsymbol{\mu}}_q^T) + \frac{\epsilon k_q}{1+\epsilon}\mathbf{e}_{q,k}^T\mathbf{J}_k^T\dot{\mathbf{J}}_k\mathbf{e}_{q,k}. \tag{49}$$

The terms involving the product $\epsilon\dot{\mathbf{J}}_k$ can be considered small and negligible. The matrix $\left(-\mathbf{K}_v - 2\epsilon\sqrt{k_q}\mathbf{I}_{6\times 6}\right)$ is symmetric and negative definite, making the associated quadratic form strictly negative. Finally, the term $-\frac{1}{1+\epsilon}\dot{\mathbf{q}}_k[\mathbf{J}_k^T\mathbf{w}_1\mathbf{J}_k]^{-1}(\bar{\boldsymbol{\mu}}_q^T + \underline{\boldsymbol{\mu}}_q^T)$ is non-positive, as indicated by Lemma 3. Consequently, this leads to $\dot{V} < 0$ due to the properties of the matrices involved. Thus, we have successfully demonstrated the intrinsic stability of the system. □

## REFERENCES


[1] A. Escande, N. Mansard, and P.-B. Wieber, "Hierarchical quadratic programming: Fast online humanoid-robot motion generation," *The International Journal of Robotics Research*, vol. 33, no. 7, pp. 1006–1028, 2014.

[2] Y. Abe, M. Da Silva, and J. Popović, "Multiobjective control with frictional contacts," in *Proceedings of the 2007 ACM SIGGRAPH/Eurographics symposium on Computer animation*, 2007, pp. 249–258.

[3] G. Raiola, C. A. Cardenas, T. S. Tadele, T. De Vries, and S. Stramigioli, "Development of a safety-and energy-aware impedance controller for collaborative robots," *IEEE Robotics and automation letters*, vol. 3, no. 2, pp. 1237–1244, 2018.

[4] J. Salini, V. Padois, and P. Bidaud, "Synthesis of complex humanoid whole-body behavior: A focus on sequencing and tasks transitions," in *2011 IEEE International Conference on Robotics and Automation*. IEEE, 2011, pp. 1283–1290.

[5] M. Liu, Y. Tan, and V. Padois, "Generalized hierarchical control," *Autonomous Robots*, vol. 40, pp. 17–31, 2016.

[6] V. Modugno, G. Neumann, E. Rueckert, G. Oriolo, J. Peters, and S. Ivaldi, "Learning soft task priorities for control of redundant robots," in *2016 IEEE International Conference on Robotics and Automation (ICRA)*. IEEE, 2016, pp. 221–226.

[7] L. Penco, E. M. Hoffman, V. Modugno, W. Gomes, J.-B. Mouret, and S. Ivaldi, "Learning robust task priorities and gains for control of redundant robots," *IEEE Robotics and Automation Letters*, vol. 5, no. 2, pp. 2626–2633, 2020.

[8] J. Silvério, S. Calinon, L. Rozo, and D. G. Caldwell, "Learning task priorities from demonstrations," *IEEE Transactions on Robotics*, vol. 35, no. 1, pp. 78–94, 2018.

[9] L. Roveda, A. Testa, A. A. Shahid, F. Braghin, and D. Piga, "Q-learning-based model predictive variable impedance control for physical human-robot collaboration," *Artificial Intelligence*, vol. 312, p. 103771, 2022.

[10] N. Dehio, R. F. Reinhart, and J. J. Steil, "Multiple task optimization with a mixture of controllers for motion generation," in *2015 IEEE/RSJ International Conference on Intelligent Robots and Systems (IROS)*. IEEE, 2015, pp. 6416–6421.

[11] V. Mnih, A. P. Badia, M. Mirza, A. Graves, T. Lillicrap, T. Harley, D. Silver, and K. Kavukcuoglu, "Asynchronous methods for deep reinforcement learning," in *International conference on machine learning*. PMLR, 2016, pp. 1928–1937.

[12] A. Ajoudani, A. M. Zanchettin, S. Ivaldi, A. Albu-Schäffer, K. Kosuge, and O. Khatib, "Progress and prospects of the human–robot collaboration," *Autonomous Robots*, vol. 42, pp. 957–975, 2018.

[13] Y. Nakamura, H. Hanafusa, and T. Yoshikawa, "Task-priority based redundancy control of robot manipulators," *The International Journal of Robotics Research*, vol. 6, no. 2, pp. 3–15, 1987.

[14] E. Mingo Hoffman, A. Laurenzi, L. Muratore, N. G. Tsagarakis, and D. G. Caldwell, "Multi-priority cartesian impedance control based on quadratic programming optimization," in *IEEE International Conference on Robotics and Automation (ICRA)*, Brisbane, Australia, May 2018, pp. 309–315.

[15] N. Dehio and J. J. Steil, "Dynamically-consistent generalized hierarchical control," in *2019 International Conference on Robotics and Automation (ICRA)*, 2019, pp. 1141–1147.

[16] F. Tassi and A. Ajoudani, "Multi-modal and adaptive control of human-robot interaction through hierarchical quadratic programming," 2023.

[17] R. Lober, V. Padois, and O. Sigaud, "Variance modulated task prioritization in whole-body control," in *2015 IEEE/RSJ International Conference on Intelligent Robots and Systems (IROS)*. IEEE, 2015, pp. 3944–3949.

[18] S. Nambiar, A. Wiberg, and M. Tarkian, "Automation of unstructured production environment by applying reinforcement learning," *Frontiers in Manufacturing Technology*, vol. 3, p. 1154263, 2023.

[19] I. Grondman, L. Busoniu, G. A. Lopes, and R. Babuska, "A survey of actor-critic reinforcement learning: Standard and natural policy gradients," *IEEE Transactions on Systems, Man, and Cybernetics, Part C (Applications and Reviews)*, vol. 42, no. 6, pp. 1291–1307, 2012.

[20] T. Degris, P. M. Pilarski, and R. S. Sutton, "Model-free reinforcement learning with continuous action in practice," in *2012 American Control Conference (ACC)*. IEEE, 2012, pp. 2177–2182.

[21] V. Mnih, A. P. Badia, M. Mirza, A. Graves, T. Lillicrap, T. Harley, D. Silver, and K. Kavukcuoglu, "Asynchronous methods for deep reinforcement learning," in *International conference on machine learning*. PMLR, 2016, pp. 1928–1937.

[22] J. X. Wang, Z. Kurth-Nelson, D. Tirumala, H. Soyer, J. Z. Leibo, R. Munos, C. Blundell, D. Kumaran, and M. Botvinick, "Learning to reinforcement learn," *arXiv preprint arXiv:1611.05763*, 2016.

[23] *Differential Kinematics and Statics*. London: Springer London, 2009, pp. 105–160. [Online]. Available: https://doi.org/10.1007/978-1-84628-642-1_3

[24] W. Chung, L.-C. Fu, and S.-H. Hsu, *Motion Control*. Berlin, Heidelberg: Springer Berlin Heidelberg, 2008, pp. 133–159. [Online]. Available: https://doi.org/10.1007/978-3-540-30301-5_7

[25] S. Caron, Q.-C. Pham, and Y. Nakamura, "Stability of surface contacts for humanoid robots: Closed-form formulae of the contact wrench cone for rectangular support areas," in *2015 IEEE International Conference on Robotics and Automation (ICRA)*. IEEE, 2015, pp. 5107–5112.

[26] A. Del Prete, "Joint position and velocity bounds in discrete-time acceleration/torque control of robot manipulators," *IEEE Robotics and Automation Letters*, vol. 3, no. 1, pp. 281–288, 2017.

[27] A. Testa, L. Raiano, M. Laghi, A. Ajoudani, and E. M. Hoffman, "Joint position bounds in resolved-acceleration control: a comparison," in *Workshop on Human-Friendly Robotics (HFR 2023)*, 2023.

[28] J. Sola, J. Deray, and D. Atchuthan, "A micro lie theory for state estimation in robotics," *arXiv preprint arXiv:1812.01537*, 2018.

[29] O. Khatib, "A unified approach for motion and force control of robot manipulators: The operational space formulation," *IEEE Journal on Robotics and Automation*, vol. 3, no. 1, pp. 43–53, 1987.

[30] R. S. Sutton and A. G. Barto, *Reinforcement learning: An introduction*. MIT press, 2018.

[31] T. Tieleman, G. Hinton, *et al.*, "Lecture 6.5-rmsprop: Divide the gradient by a running average of its recent magnitude," *COURSERA: Neural networks for machine learning*, vol. 4, no. 2, pp. 26–31, 2012.

[32] N. M. Aszemi and P. Dominic, "Hyperparameter optimization in convolutional neural network using genetic algorithms," *International Journal of Advanced Computer Science and Applications*, vol. 10, no. 6, 2019.

[33] H. Alibrahim and S. A. Ludwig, "Hyperparameter optimization: Comparing genetic algorithm against grid search and bayesian optimization," in *2021 IEEE Congress on Evolutionary Computation (CEC)*. IEEE, 2021, pp. 1551–1559.

[34] T. Tang, H.-C. Lin, Y. Zhao, W. Chen, and M. Tomizuka, "Autonomous alignment of peg and hole by force/torque measurement for robotic assembly," in *2016 IEEE international conference on automation science and engineering (CASE)*. IEEE, 2016, pp. 162–167.

[35] J. Song, Q. Chen, and Z. Li, "A peg-in-hole robot assembly system based on gauss mixture model," *Robotics and Computer-Integrated Manufacturing*, vol. 67, p. 101996, 2021.

[36] K. Nottensteiner, F. Stulp, and A. Albu-Schäffer, "Robust, locally guided peg-in-hole using impedance-controlled robots," in *2020 IEEE International Conference on Robotics and Automation (ICRA)*. IEEE, 2020, pp. 5771–5777.

[37] H. W. Kuhn and A. W. Tucker, "Nonlinear programming," in *Traces and emergence of nonlinear programming*. Springer, 2013, pp. 247–258.

[38] B. Siciliano, O. Khatib, and T. Kröger, *Springer handbook of robotics*. Springer, 2008, vol. 200.